Present-day deformation of the Pyrenees revealed by GPS surveying and earthquake focal mechanisms until 2011

A. Rigo, Philippe Vernant, K. L. Feigl, X. Goula, G. Khazaradze, J. Talaya, Laurent Morel, Jean-Marie Nicolas, S. Baize, Jean Chery, et al.

Geophysical Journal International

Geophys. J. Int. (2015) **201,** 947–964
GJI Geodynamics and tectonics

doi: 10.1093/gji/ggv052

Present-day deformation of the Pyrenees revealed by GPS surveying and earthquake focal mechanisms until 2011

A. Rigo,[1,*] P. Vernant,[2] K. L. Feigl,[3] X. Goula,[4] G. Khazaradze,[5] J. Talaya,[4] L. Morel,[6] J. Nicolas,[6] S. Baize,[7] J. Chéry[2] and M. Sylvander[1]

[1] *Institut de Recherche en Astrophysique et Planétologie, Université de Toulouse, CNRS, Observatoire Midi-Pyrénées,* 14 *ave. Edouard Belin, F-*31400 *Toulouse, France. E-mail: Alexis.Rigo@irap.omp.eu*
[2] *Laboratoire Géosciences Montpellier, Université Montpellier II-CNRS, Pl. E. Bataillon, F-*34095 *Montpellier Cedex* 05*, France*
[3] *Department of Geoscience, University of Wisconsin, Madison, WI* 53706*, USA*
[4] *Institut Cartogràfic i Geològic de Catalunya (ICGC), E-*08038 *Barcelona, Spain*
[5] *Universitat de Barcelona, E-*08028 *Barcelona, Spain*
[6] *Laboratoire de Géodésie et Géomatique, ESGT-CNAM, F-*72000 *Le Mans, France*
[7] *Institut de Radioprotection et de Sureté Nucléaire, F-*92260 *Fontenay-aux-Roses, France*

Accepted 2015 February 2. Received 2015 February 2; in original form 2013 July 29

SUMMARY

The Pyrenean mountain range is a slowly deforming belt with continuous and moderate seismic activity. To quantify its deformation field, we present the velocity field estimated from a GPS survey of the Pyrenees spanning 18 yr. The PotSis and ResPyr networks, including a total of 85 GPS sites, were installed and first measured in 1992 and 1995–1997, respectively, and remeasured in 2008 and 2010. We obtain a deformation field with velocities less than 1 mm yr^{-1} across the range. The estimated velocities for individual stations do not differ significantly from zero with 95 per cent confidence. Even so, we estimate a maximum extensional horizontal strain rate of 2.0 ± 1.7 nanostrain per year in a N–S direction in the western part of the range. We do not interpret the vertical displacements due to their large uncertainties. In order to compare the horizontal strain rates with the seismic activity, we analyse a set of 194 focal mechanisms using three methods: (i) the 'r' factor relating their P and T axes, (ii) the stress tensors obtained by fault slip inversion and (iii) the strain-rate tensors. Stress and strain-rate tensors are estimated for: (i) the whole data set, (ii) the eastern and western parts of the range separately, and (iii) eight zones, which are defined based on the seismicity and the tectonic patterns of the Pyrenees. Each of these analyses reveals a lateral variation of the deformation style from compression and extension in the east to extension and strike-slip in the west of the range. Although the horizontal components of the strain-rate tensors estimated from the seismic data are slightly smaller in magnitude than those computed from the GPS velocity field, they are consistent within the 2σ uncertainties. Furthermore, the orientations of their principal axes agree with the mapped active faults.

Key words: Space geodetic surveys; Seismicity and tectonics; Continental tectonics: extensional; Dynamics: seismotectonics; Europe.

1 INTRODUCTION

The Pyrenees are a mountain belt along the French-Spanish border, where the rate of deformation is low and the seismicity is continuous and moderate (Souriau & Pauchet 1998; Fig. 1a). However, historical earthquakes with probable magnitudes as high as 6.0–6.5 have been inferred from a seismic sequence with intensity *VII–IX* in 1427–1428 in the eastern Pyrenees near Olot (Briais *et al.* 1990; Olivera *et al.* 2006; Perea 2009) and an earthquake with intensity *VIII* in 1660 near Lourdes in the central part (Lambert & Levret-Albaret 1996). In order to characterize and to quantify the present-day Pyrenean deformation, we present a velocity field obtained from two GPS networks encompassing the whole Pyrenean range that were surveyed several times between 1992 and 2010.

In addition to quantifying the deformation field in the Pyrenees, these two GPS networks may provide answers to questions that have emerged since their installation 20 yr ago especially about N–S

*Now at: Laboratoire de Géologie, ENS, CNRS, PSL Research University, 24 rue Lhomond, F75231 Paris Cedex 5, France. E-mail: alexis.rigo@ens.fr.

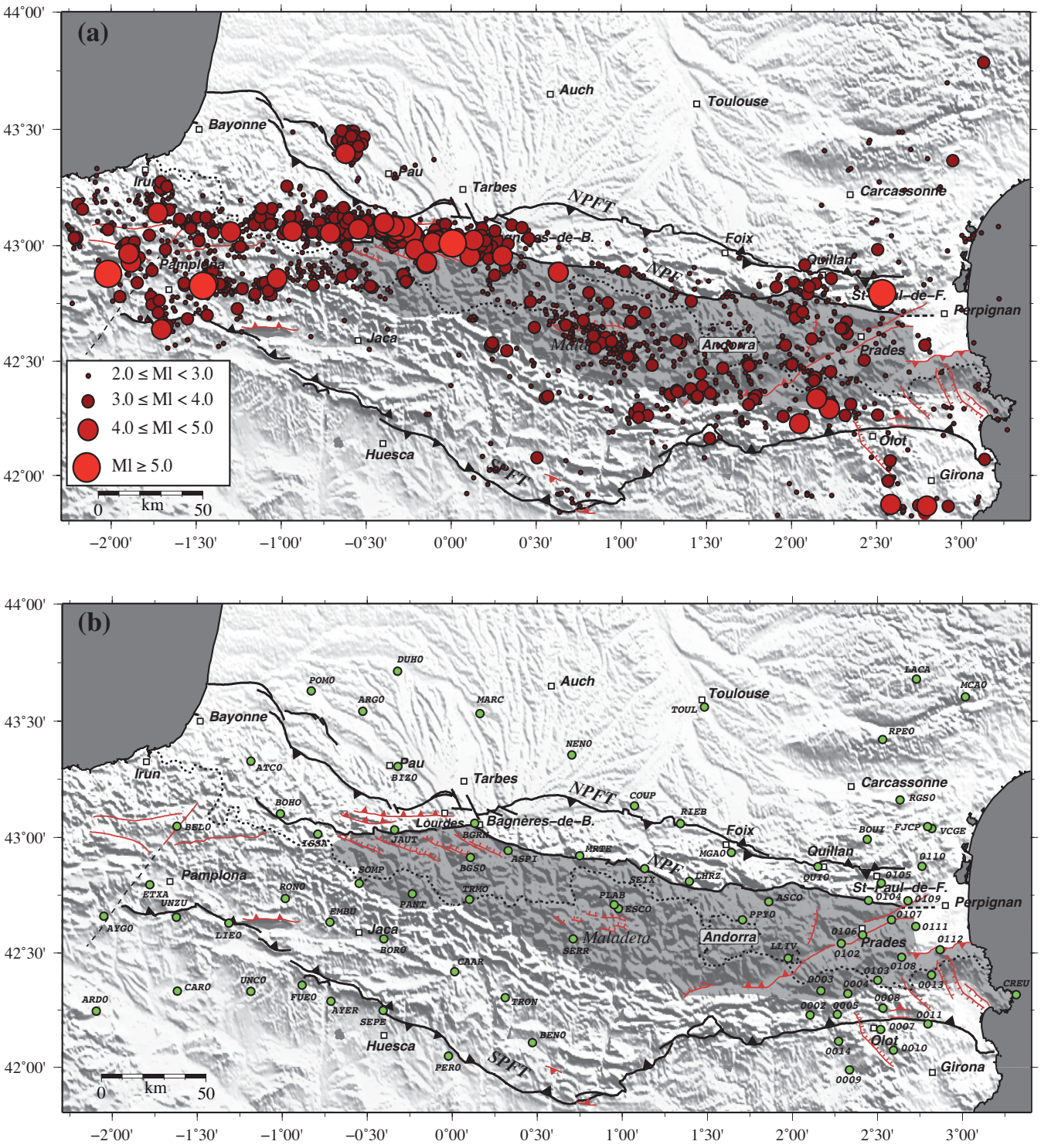

Figure 1. Seismotectonic maps of Pyrenees on the shaded relief. In black the main faults of the range: NPFT, North Pyrenean Frontal thrust; NPF, North Pyrenean Fault; SPFT, South Pyrenean Frontal Thrust. Grey area, Palaeozoic domain. In red the faults considered as active at present time from Lacan & Ortuño (2012). (a) Seismicity for the period 1989–2011. (b) GPS points of the PotSis and ResPyr networks for which velocities have been determined after the measurements done in 2008 and 2010.

extension suggested by recent studies (e.g. Nocquet & Calais 2004; de Vicente *et al.* 2008; Chevrot *et al.* 2011; Asensio *et al.* 2012): Is this extension uniform throughout the range? Is this extension mainly revealed by normal fault plane solutions, the expression of horizontal movements or, maybe, principally of vertical movements as suggested by Lacan & Ortuño (2012) and Vernant *et al.* (2013)? Is it now possible to obtain a coherent stress field in the Pyrenees when others had failed until now, leaving it an open question (Nicolas *et al.* 1990; Delouis *et al.* 1993; Souriau *et al.* 2001; de Vicente *et al.* 2008; Stich *et al.* 2010)?

Our estimated GPS velocity field is compared with the tectonics and seismicity of the range. In particular, we focus on the stress and strain-rate tensors determined from an updated compilation of the focal mechanisms.

2 SEISMOTECTONIC SETTING

2.1 Pyrenean tectonics

The Pyrenees result from the convergence of the Iberian Plate and the Eurasian Plate. The convergence started 65 Ma ago, following a period of extension (−115 to −80 Ma) related to the opening of the Bay of Biscay to the west (e.g. Jammes *et al.* 2010). The eastern part has been affected by Mediterranean tectonics and the opening of the Gulf of Lion 30 Ma ago as reviewed by Choukroune (1992) and Vissers & Meijer (2012). From north to south, the main tectonic structures running E–W along the mountain range include: (1) the north Pyrenean frontal thrust (NPFT) overlapping the sedimentary Aquitaine Basin to the north, (2) the north Pyrenean fault (NPF), separating the Iberian and Eurasian Plates and (3) the south Pyrenean frontal thrust (SPFT) overlapping the Ebro Basin to the south (Fig. 1). The NPF is the northern limit of the axial zone constituting a Palaeozoic domain (grey area in Fig. 1), and coincides at depth to a step in the Moho of 15–20 km, with the thicker crust below the Iberian part of the range (Hirn *et al.* 1980). The Moho step progressively decreases in magnitude from west to east and vanishes below the Mediterranean Sea. The structure of the Pyrenees has been analysed by several methods, including: refraction and reflection seismic experiments (e.g. Gallart *et al.* 1981; Daignières *et al.* 1994), gravimetric studies and modelling (Torné *et al.* 1989; Vacher & Souriau 2001), lithospheric tomography with seismological methods (Souriau & Granet 1995; Souriau *et al.* 2008; Chevrot *et al.* 2014), and geoelectrical and magnetotelluric methods (Pous *et al.* 1995; Ledo *et al.* 2000; Campanyà *et al.* 2011, 2012). Although the Pyrenean structure is relatively well known at the scale of the range, the characterization of the structures that are tectonically active at the present time is still a matter of debate. The main E–W faults described above (NPF, NPFT and SPFT) show no evidence of recent activity in the field. The faults identified as active by Lacan & Ortuño (2012) are shown in red in Fig. 1. Both the activity and the mode of deformation of these faults are controversial. For example, in the easternmost part of the Pyrenees, the Têt and Tech faults are considered as normal faults by some authors (e.g. Briais *et al.* 1990) or as reverse, strike-slip or inactive by others (e.g. Philip *et al.* 1992; Calvet 1999; Goula *et al.* 1999; Carozza & Delcaillau 2000). Geomorphological investigations identified E–W extensional active faults in the axial zone (Fig. 1b), especially in the Maladeta massif and near the city of Lourdes (Alasset & Meghraoui 2005; Dubos-Sallée *et al.* 2007; Ortuño *et al.* 2008; Lacan & Ortuño 2012). To the west of Lourdes, thrust faulting prevails, indicating a compressive regime (Lacan *et al.* 2012; Fig. 1). According to Lacan & Ortuño (2012), deformation at the present time in the Pyrenees is governed by strike-slip in their western part, by north–south compression with reverse faulting in the northern part of the central Pyrenees. In the axial zone (i.e. the part of the Pyrenees where the topographic elevation reaches 3000 m), deformation occurs on E-W striking en echelon normal faults, indicating N–S extension. This extension is also clearly expressed by the focal mechanisms of earthquakes (Fig. 4; Chevrot *et al.* 2011) and the stress tensors determined by de Vicente *et al.* (2008).

2.2 Seismicity

Fig. 1(a) shows the seismicity between 1989 and 2011, as compiled by the Observatoire Midi-Pyrénées (OMP) and the Institut Cartogràfic i Geològic de Catalunya (ICGC). The seismic activity is continuous with more than 15 000 moderate events with magnitudes less than 5.5. Most of the events are located in the upper crust with depths less than 15 km. The deepest events with depth 23–25 km occur in the western part of the belt.

Two important clusters are not considered in the following because they were induced by human activity. The cluster located to the west of the city of Pau is related to production of natural gas in the Lacq gas field (Bardainne *et al.* 2008). The E–W elongated cluster (between 1° W and 1° 24′W) east to the city of Pamplona (Spain) is mainly but not entirely related to the water impounded behind the Itoiz dam beginning in 2004 (Ruiz *et al.* 2006a; Durá-Gómez & Talwani 2010).

The pattern of the seismicity shows a dichotomy between the eastern and the western parts of the range, as suggested earlier (Souriau & Pauchet 1998). In the western part, the seismicity is concentrated along a linear band of at least 30 km width. On N–S cross-sections, the seismicity dips to the north at 55–60° down to 25 km depth (Gagnepain-Beyneix 1987; Rigo *et al.* 2005). This seismicity is not clearly associated with crustal faults mapped in the belt and the NPF seems to be seismically inactive. The most significant events were the M 5.3–5.7 Arette earthquake in 1967 (Hoang Trong & Rouland 1971), the M_{l} 5.1 Arudy earthquake in 1980 (Gagnepain-Beyneix *et al.* 1982) and M_{l} 5.0 Argelès-Gazost earthquake in 2006 (Sylvander *et al.* 2008).

In the eastern part of the range, the seismicity is more diffuse and less prominent than in the west. In the Maladeta area, the seismicity is fairly dense and active normal faults have been identified in the field. The most recent significant earthquake occurred in 1996 near the city of St-Paul-de-Fenouillet with a magnitude M_{l} 5.2 (Rigo *et al.* 1997; Pauchet *et al.* 1999; Rigo & Massonnet 1999; Rigo 2010).

2.3 Previous geodetic studies

In 1992, the PotSis GPS network was installed in the easternmost part of the Pyrenees in order to survey the area affected by the 1427–1428 seismic sequence (Briais *et al.* 1990; Goula *et al.* 1996; Lambert & Levret 1996; Olivera *et al.* 2006; Lacan & Ortuño 2012). In 1995 and 1997, we installed the ResPyr network covering the entire Pyrenees range in order to characterize and quantify its internal deformation. At that time, the deformation rate of Pyrenees had not been measured directly. The deformation pattern expected was N–S compression, according to geological and geodynamical considerations over time scales of 10 Myr. Surprisingly, the first GPS measurement of deformation across the Pyrenees yielded extension at a rate of 0.5 ± 0.5 mm yr^{-1} (Nocquet & Calais 2004). The large uncertainty was due to the inclusion of only a single continuous GPS site on the Spanish side of the range. Nocquet (2012) updated this rate to a value less than 0.2 mm yr^{-1}. However, studying the kinematics of the Iberia-Maghreb Plate boundary, Stich *et al.* (2006) reported southward velocities at 1.0 ± 0.6 mm yr^{-1} with respect to Europe of continuous GPS stations LLIV and ESCO (Fig. 8) on the Spanish side of the Pyrenees. Another recent study (Asensio *et al.* 2012), based on continuous GPS observations over 3.5 yr at 35 sites, shows that the stations south of the western and central Pyrenees move away from the stable part of western Europe with a velocity of 0.5 to 1.5 mm yr^{-1}. A NNE–SSW profile across the

western Pyrenees indicates extension at 2.5 ± 0.5 nstrain yr^{-1}. If we assume the width of the Pyrenees to be 100–150 km, then this strain rate would be equivalent to 0.3–0.4 mm yr^{-1} of extension.

3 GPS DATA AND ANALYSIS

3.1 GPS campaigns

Two GPS networks were installed in the Pyrenees in three phases during the 1990s (Fig. 1b). The PotSis network, covering the eastern part of the range with a 20 km average distance between sites, was installed and measured for the first time in 1992 (Talaya *et al.* 1999). Each of the 24 sites was surveyed four times: in 1992, 1994, 1999 and 2006. Some stations were also surveyed in 1996 following the M_l 5.2 earthquake of St-Paul-de-Fenouillet (Rigo *et al.* 1997).

The ResPyr network, covering the whole Pyrenees and the northern and southern forelands, was installed and first measured in 1995 from the Mediterranean Sea to the centre of the range (at the city of Bagnères-de-Bigorre, site BGRN), and in 1997 from the centre to the Atlantic Ocean and for the forelands (Fig. 1b; Fleta *et al.* 1996). The ResPyr network is composed of 70 stations from which nine are common to the PotSis network, with an average spacing of 50 km. In 1995 and 1997, the satellites' signals were recorded at each site during three evening sessions of at least 8 hr.

Both networks were re-surveyed in 2008 and 2010 with sessions of 36–72 hr (Table 1). Given the long time span between the first and the last surveys, several different types of receivers (Trimble 4000SST, SSE and NetRS; Ashtech XII, Z-XII, Z-X, L-XII, LM-XII and UZ-XII; Rogue SNR-8100) and antennas (Trimble models 14 532.00, 14 532.10, 22 020–00, 29 659.00, 41 249.00; Ashtech models 70 0228D, 70 0936A, 70 1975.01A, 70 0228A, 70 1945–01 and a Rogue antenna with choke rings) were used. The 74 sites observed are given in Table 1. The sites with names starting with '0' use a constrained centring technique on pillars. The others were surveyed using tripods. The tripod setup can be subject to centring errors of up to ∼2 mm, inducing velocity errors of less than 0.2 mm yr^{-1} over time spans of more than 10 yr. Anomalously high velocities relative to the surrounding points were obtained due to local instabilities or due to identified mistakes by the operators. These aberrant measurements are not shown or discussed in the following.

3.2 Data analysis

We use the GAMIT/GLOBK software package (http://www-gpsg.mit.edu) to compute the coordinates and velocities of the surveyed GPS sites using a three-step strategy (Feigl *et al.* 1993; Dong *et al.* 1998). To tie our local network to the ITRF reference frame, we include GPS data from 18 International GNSS Service (IGS) stations, when available (BELL, CAGL, CANT, CREU, EBRE, ESCO, GRAS, LLIV, MADR, MARS, MTPL, POTS, SFER, TLSE, VILL, WSRT, WETT, ZIMM). No IGS sites were available in 1992, but in 1994, nine sites were already available (BELL, CREU, EBRE, ESCO, LLIV, MADR, TLSE, WETT and ZIMM). The two continuous GNSS sites close to our network were also added to the analysis (LACA and FJCP). Following Reilinger *et al.* (2006), we account for temporally correlated noise in each continuous GPS time series by using the first-order Gauss-Markov extrapolation (FOGMEX) algorithm proposed by Herring (2003) to determine a random-walk noise term, which we then incorporated into the Kalman filter used to estimate the velocities. For the episodically measured sites, we apply a random-walk of 1 mm sqrt(yr)$^{-1}$, equal to the average of values obtained for 320 continuous GPS stations globally distributed with time series spans ranging from 2.5 to 17 yr. Velocities and their 1σ uncertainties were estimated in the ITRF2008 reference frame and then transformed into the Eurasian reference frame by minimizing the horizontal velocities of the survey sites and the IGS stations located on the Eurasian Plate (BELL, CAGL, CANT, CREU, EBRE, ESCO, GRAS, LLIV, MADR, MARS, MTPL, POTS, TLSE, VILL, WSRT, WETT, ZIMM). The velocities in the Eurasia reference frame are given in Table 2. The WRMS value for the horizontal velocity residuals of these 93 sites is 0.11 mm yr^{-1}. The velocities with 95 per cent confidence ellipses are shown in Fig. 2.

4 VELOCITY FIELD

We finally obtain a set of 80 velocity vectors (74 campaign stations plus six continuous stations) covering the whole Pyrenean range and the forelands. We do not interpret the vertical velocities because their uncertainties are large. The time spans vary from 18 yr for PotSis (the easternmost and densest network), to 15 yr and 13 yr for the eastern and western parts of ResPyr, respectively. Most of the velocities are smaller than their uncertainties. Their directions are variable, making it difficult to characterize a general trend of the deformation in the Pyrenees. Averaged over the entire network, the velocity components $V_E = -0.3 \pm 0.3$ mm yr^{-1} ($\pm 1\sigma$) and $V_N = 0.0 \pm 0.3$ mm yr^{-1} ($\pm 1\sigma$) seem to suggest a westward motion of the Pyrenees with respect to Eurasia. However, this motion is concentrated in the centre part of the network (Fig. 2), which was first measured during two campaigns in 1995 and 1997. In 1995, the measured sites were at longitudes east of 0°E and in 1997, west of 0°E. This configuration may have induced a bias, generating this apparent localized westward motion and we consider it as insignificant.

To interpret the velocity field, we compute five N–S profiles perpendicular to the E–W Pyrenean tectonic frame, and one E–W profile, as indicated by arrows in Fig. 2. Each N–S profile has a half-width of projection of 45 km. The E–W profile includes all the points. We show the profiles in Fig. 3 with their corresponding topographic elevations. Profiles AA′ to DD′ exhibit small strain rates from 0.0 to 0.8 nstrain yr^{-1} with uncertainties ranging from 1.1 to 1.7 nstrain yr^{-1}. The westernmost profile (EE′) indicates N–S extension at a rate of 2.0 ± 1.8 nstrain yr^{-1}. Our results are compatible with the 2.5 ± 0.5 nstrain yr^{-1} estimated by Asensio *et al.* (2012) for the western part of the range from a 3.5-yr span of continuous GPS data.

5 FOCAL MECHANISMS

The Pyrenees are shaken by a few hundred earthquakes every year. The maximum magnitude recorded during the last 50 yr is $M_l = 5.7$ for the 1967 Arette earthquake (date 19670813 in the table of Appendix Supplementary material). The last major events were the $M_l = 5.2$ St-Paul-de-Fenouillet earthquake in 1996 (date 19960218 in the table of appendix; Rigo *et al.* 1997; Pauchet *et al.* 1999; Rigo 2010) and the $M_l = 5.0$ Lourdes event in 2006 (date 20061117 in the table of Appendix Supplementary material; Sylvander *et al.* 2008). In order to compare qualitatively and quantitatively the deformation fields inferred from the seismic and geodetic observations, we analyse the available focal mechanisms. Several previous studies have used fewer than ten normal faulting mechanisms to argue for north–south extension across the Pyrenees (de Vicente *et al.* 2008; Stich *et al.* 2010; Chevrot *et al.* 2011; Asensio *et al.* 2012). Using

Table 1. Schedule of occupation of the PotSis and ResPyr GPS Pyrenean sites.

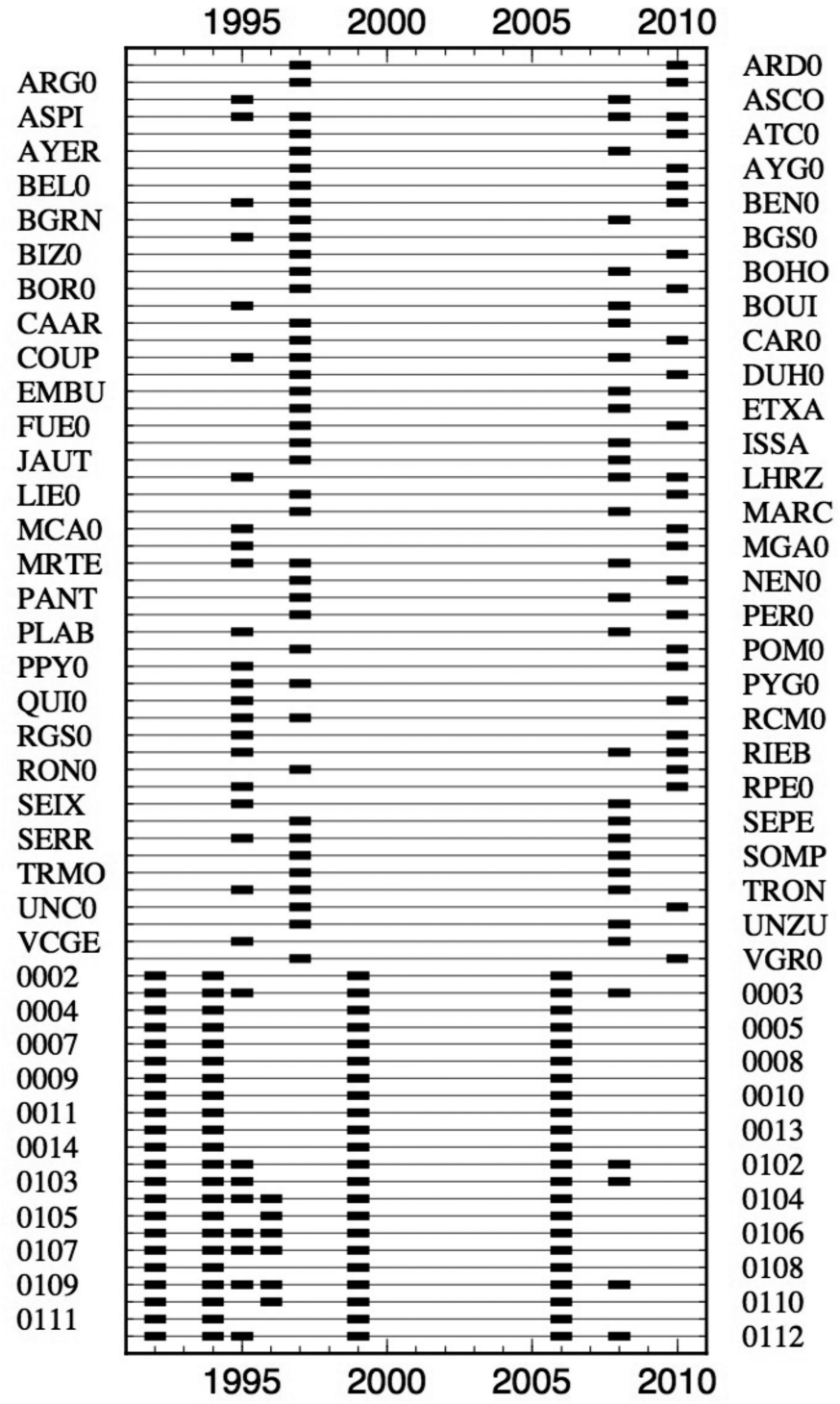

three different methodologies in analysing the focal mechanisms, we seek to constrain the stress field when others failed (Nicolas *et al.* 1990; Delouis *et al.* 1993). Does claimed N–S extension apply to the whole range or is it restricted to some areas?

Our set of Pyrenean focal solutions is constituted by the best-constrained data set of Souriau *et al.* (2001). It has been updated to include the focal mechanisms from Dubos *et al.* (2004), Ruiz *et al.* (2006b), Sylvander *et al.* (2008), and Chevrot *et al.* (2011) (Appendix Supplementary material). Thus, we obtain a final set of 194 focal mechanisms from 1967 to 2010 with local magnitudes (M_l) ranging from 1.5 to 5.7 (Fig. 4). Like the seismicity, the focal solutions are concentrated in the western part of the range and diffuse elsewhere. All types of mechanisms are present: reverse faulting principally at the eastern and central parts of the range with N–S and NW–SE striking nodal planes; strike-slip faulting both right-lateral and left-lateral everywhere; and normal faulting

Table 2. Coordinates and velocities (mm yr^{-1}) with 1σ uncertainties of the 74 GPS pyrenean sites of the ResPyr and PotSis networks plus the 19 permanent GPS sites used for the transformation of the velocities into the Eurasian reference frame. V_E: east component; V_N: north component; ρ: correlation coefficient between east and north components.

Site	Longitude	Latitude	V_E	$\pm1\sigma$	V_N	$\pm1\sigma$	ρ
ARD0	−2.10	42.25	−0.74	0.32	0.56	0.32	−0.005
ARG0	−0.53	43.54	−0.21	0.32	−0.07	0.32	−0.006
ASCO	1.86	42.72	−0.91	0.32	−0.30	0.32	−0.005
ASPI	0.33	42.94	−0.34	0.30	−0.19	0.30	−0.003
ATC0	−1.19	43.33	−0.35	0.31	0.43	0.32	−0.002
AYER	−0.72	42.29	0.06	0.35	0.10	0.35	−0.004
AYG0	−2.05	42.66	0.30	0.32	−0.25	0.32	−0.003
BEL0	−1.62	43.05	−0.30	0.31	0.57	0.32	0.000
BEN0	0.47	42.11	−0.46	0.30	−0.01	0.30	−0.007
BGRN	0.13	43.06	−0.82	0.33	−0.18	0.34	−0.003
BGS0	0.10	42.91	−0.50	0.33	−0.10	0.32	−0.012
BIZ0	−0.32	43.31	0.06	0.34	0.41	0.33	−0.009
BOHO	−1.01	43.10	−0.15	0.34	−0.09	0.34	−0.001
BOR0	−0.40	42.56	−0.22	0.31	−0.31	0.32	−0.001
BOUI	2.44	43.00	−0.30	0.31	−0.14	0.31	−0.010
CAAR	0.01	42.42	0.19	0.34	−0.06	0.34	−0.003
CAR0	−1.62	42.33	−0.38	0.31	−0.32	0.32	0.000
COUP	1.07	43.14	−0.81	0.32	−0.11	0.32	0.009
DUH0	−0.32	43.71	0.14	0.32	−0.13	0.32	−0.002
EMBU	−0.72	42.63	−0.85	0.39	−0.34	0.40	0.024
ETXA	−1.78	42.80	−0.58	0.34	0.08	0.35	−0.002
FUE0	−0.88	42.36	−0.39	0.32	0.16	0.32	−0.006
ISSA	−0.79	43.02	0.20	0.34	0.18	0.35	−0.004
JAUT	−0.34	43.03	−0.88	0.35	0.48	0.36	−0.007
LHRZ	1.39	42.81	−0.06	0.30	−0.42	0.30	−0.008
LIE0	−1.32	42.63	0.02	0.31	0.11	0.32	−0.001
MARC	0.16	43.53	−0.28	0.35	−0.13	0.37	−0.026
MCA0	3.02	43.60	−0.64	0.29	0.25	0.30	−0.006
MGA0	1.64	42.94	−0.85	0.30	0.16	0.30	0.008
MRTE	0.75	42.92	−0.67	0.32	0.26	0.33	−0.007
NEN0	0.70	43.36	−0.41	0.32	0.19	0.33	−0.002
PANT	−0.24	42.76	−0.01	0.34	−0.32	0.35	−0.004
PER0	−0.02	42.05	0.11	0.32	0.15	0.32	−0.003
PLAB	0.95	42.71	0.17	0.33	−0.13	0.32	−0.016
POM0	−0.83	43.63	0.21	0.32	−0.01	0.32	−0.001
PPY0	1.71	42.64	1.05	0.33	0.42	0.30	−0.016
PYG0	0.46	42.77	−2.92	1.09	1.55	1.11	−0.055
QUI0	2.15	42.87	−0.22	0.31	0.04	0.30	−0.019
RGS0	2.63	43.16	0.07	0.29	−0.29	0.29	−0.006
RIEB	1.34	43.06	−0.16	0.30	−0.15	0.30	−0.011
RON0	−0.98	42.74	−0.09	0.32	0.21	0.32	−0.002
RPE0	2.53	43.42	−0.70	0.31	−0.34	0.31	−0.017
SEIX	1.13	42.87	−0.13	0.33	−0.29	0.32	−0.014
SEPE	−0.41	42.25	0.58	0.37	−0.29	0.35	−0.018
SERR	0.71	42.56	0.05	0.32	−0.53	0.32	−0.011
SOMP	−0.55	42.80	−0.69	0.34	−0.20	0.34	−0.001
TRMO	0.10	42.73	−0.69	0.31	−0.01	0.31	−0.001
TRON	0.31	42.31	−0.45	0.32	−0.59	0.32	−0.014
UNC0	−1.19	42.33	−0.43	0.33	0.00	0.33	−0.005
UNZU	−1.63	42.66	0.21	0.36	−0.40	0.36	−0.008
VCGE	2.82	43.04	−0.11	0.31	−0.42	0.31	0.000
VGR0	−2.53	42.31	−0.61	0.31	0.12	0.31	0.000
0002	2.10	42.23	−0.18	0.32	−0.19	0.32	0.012
0003	2.17	42.34	−0.43	0.29	0.05	0.29	0.004
0004	2.32	42.32	−0.56	0.32	−0.04	0.32	0.011
0005	2.26	42.23	−0.35	0.31	0.10	0.31	0.008
0007	2.52	42.17	0.02	0.31	0.03	0.31	0.006
0008	2.53	42.26	−0.01	0.31	−0.16	0.31	0.007
0009	2.33	41.99	−0.13	0.31	−0.12	0.31	0.009
0010	2.59	42.08	0.08	0.31	0.18	0.31	0.005
0011	2.80	42.19	0.12	0.31	−0.15	0.31	0.005

Table 2 (*Continued.*)

Site	Longitude	Latitude	V_E	$\pm1\sigma$	V_N	$\pm1\sigma$	ρ
0013	2.82	42.40	−0.15	0.33	0.27	0.32	0.024
0014	2.27	42.12	0.06	0.31	−0.05	0.31	0.007
0102	2.29	42.54	−0.06	0.30	0.23	0.30	0.003
0103	2.50	42.38	−0.63	0.29	0.40	0.29	0.008
0104	2.45	42.73	−0.37	0.32	−0.09	0.32	0.012
0105	2.52	42.80	−0.20	0.32	−0.26	0.32	0.008
0106	2.41	42.58	−0.04	0.33	0.15	0.33	0.007
0107	2.58	42.64	−0.19	0.31	−0.19	0.31	0.009
0108	2.64	42.48	−0.16	0.33	0.60	0.34	0.009
0109	2.68	42.73	−0.77	0.30	0.25	0.31	0.002
0110	2.76	42.88	−0.19	0.32	−0.07	0.32	0.012
0111	2.72	42.62	−0.66	0.32	−0.08	0.32	0.013
0112	2.87	42.51	−0.21	0.30	0.55	0.31	0.001
BELL	1.40	41.60	−0.33	0.33	−0.03	0.33	0.000
CAGL	8.97	39.14	−0.37	0.32	0.03	0.32	0.011
CANT	−3.80	43.47	−0.93	0.37	0.22	0.37	0.001
CREU	3.32	42.32	−0.45	0.32	−0.07	0.32	0.002
EBRE	0.49	40.82	−0.10	0.28	−0.34	0.28	0.001
ESCO	0.98	42.69	−0.98	0.37	0.26	0.37	0.001
FJCP	2.80	43.05	−0.46	0.44	0.44	0.44	0.001
GRAS	6.92	43.76	−0.15	0.15	0.22	0.15	0.067
LACA	2.73	43.68	−0.26	0.46	0.57	0.46	0.002
LLIV	1.97	42.48	−0.40	0.36	−0.05	0.36	0.001
MADR	−4.25	40.43	−0.01	0.17	−0.41	0.17	0.009
MARS	5.35	43.28	−0.65	0.32	0.11	0.32	0.003
MTPL	3.87	43.64	0.05	0.32	−0.02	0.32	0.002
POTS	13.07	52.38	−0.38	0.04	−0.15	0.04	0.354
TLSE	1.48	43.56	−0.16	0.36	0.11	0.36	0.001
VILL	−3.95	40.44	−0.13	0.18	0.31	0.18	0.011
WETT	12.88	49.14	1.35	0.77	1.35	0.74	0.075
WSRT	6.60	52.92	−0.07	0.32	0.33	0.32	0.000
ZIMM	7.47	46.88	0.01	0.20	0.19	0.20	0.009

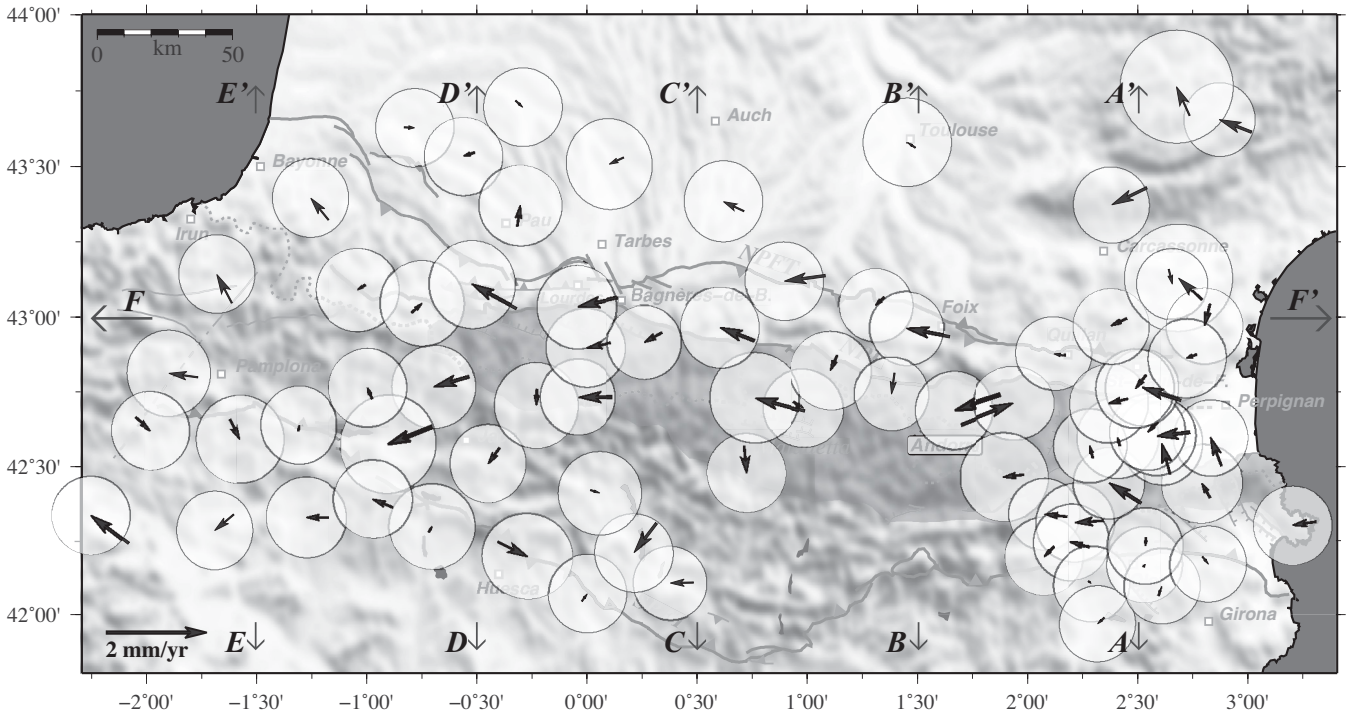

Figure 2. GPS horizontal velocity field into the Eurasian reference frame (Table 2) with their 95 per cent confidence ellipses superimposed on the shaded topographic map of Pyrenees. Arrows with letters from AA′ to FF′ locate the profiles of Fig. 3.

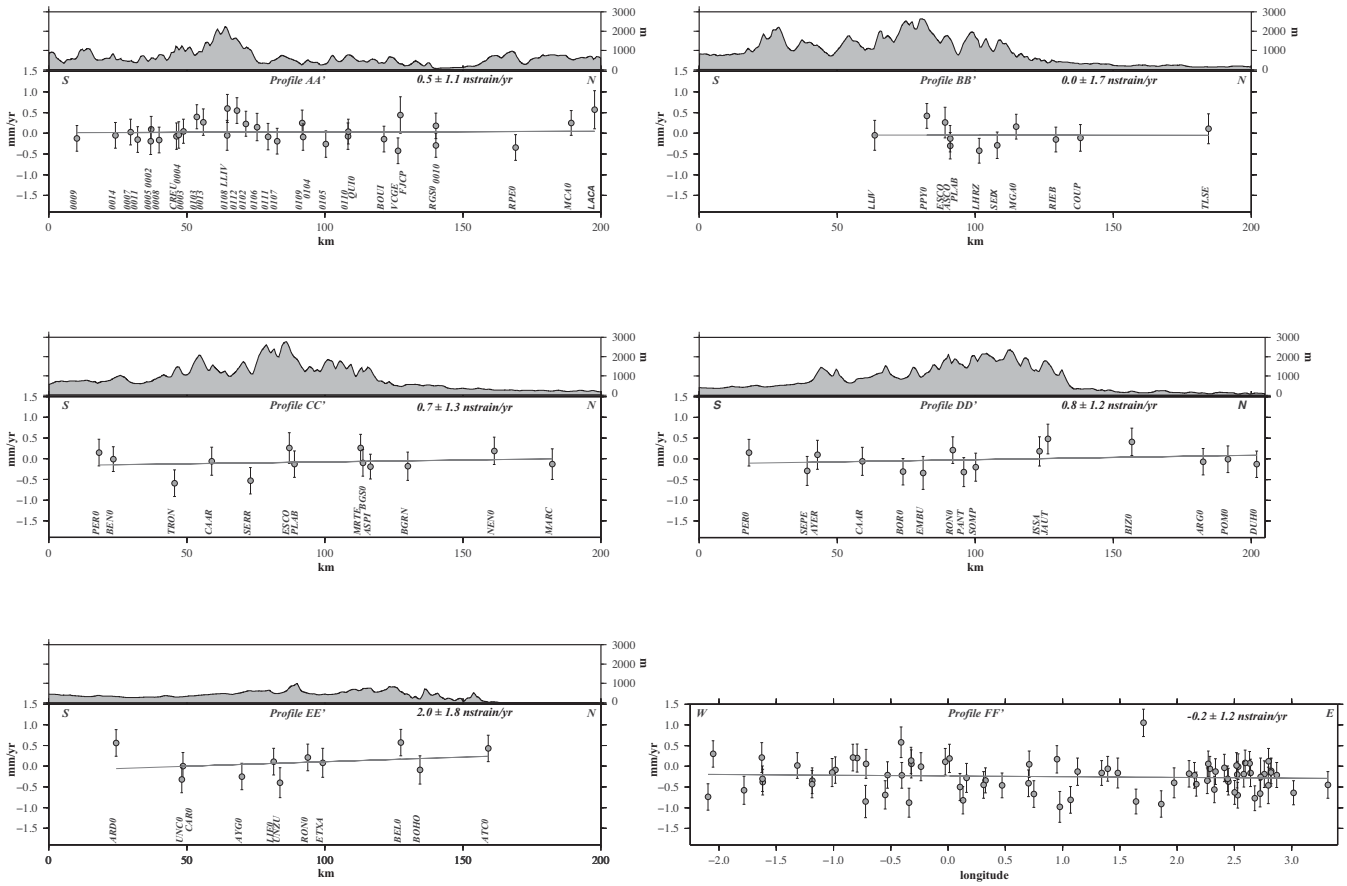

Figure 3. N–S (AA′ to EE′) and E–W (FF′) profiles located in Fig. 2 with the projected GPS velocities and their 1σ uncertainties. For the N–S profiles, the half-width of projection is 45 km and all the GPS velocities are projected on the E–W profile. At each profile, the corresponding topographic envelope and deformation rate are done.

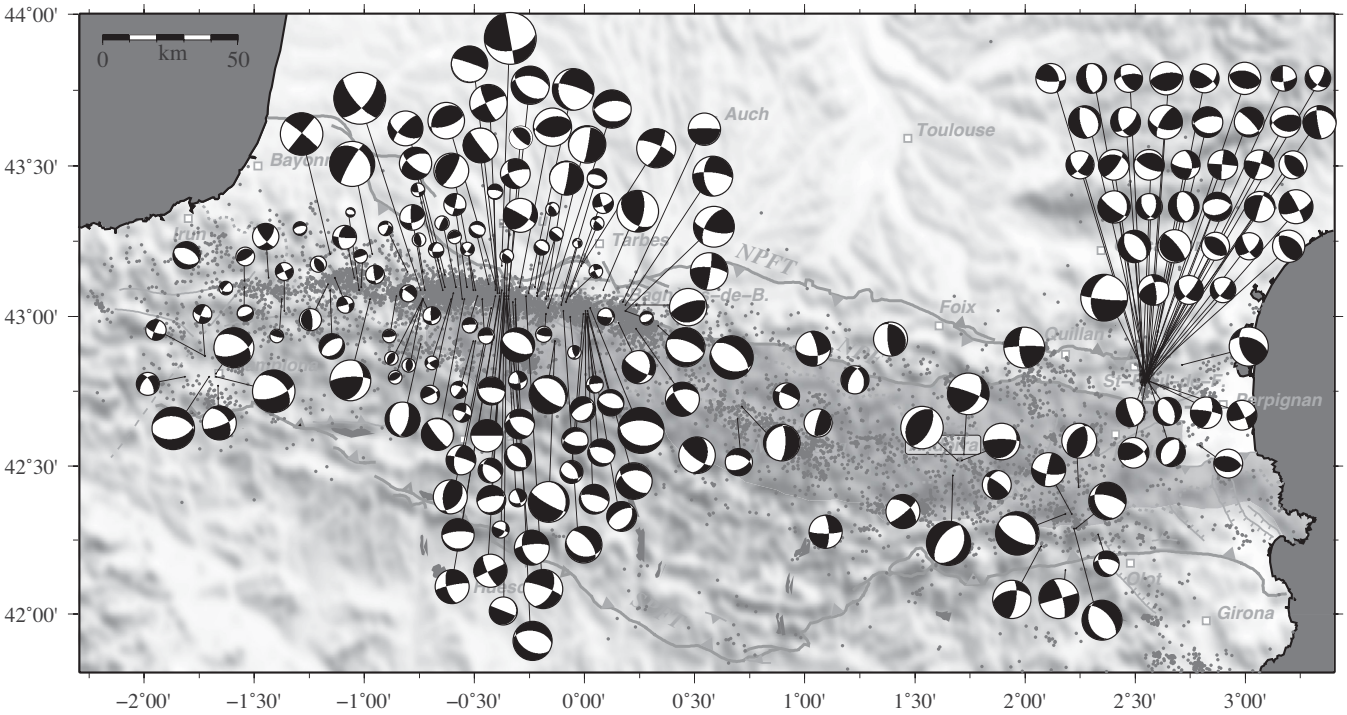

Figure 4. Focal mechanisms over the period 1967–2011 (Appendix Supplementary material) on the shaded topographic map of Pyrenees. The size of the focal mechanisms is proportional to the magnitude. The 1989–2011 seismicity and the faults are reported in grey.

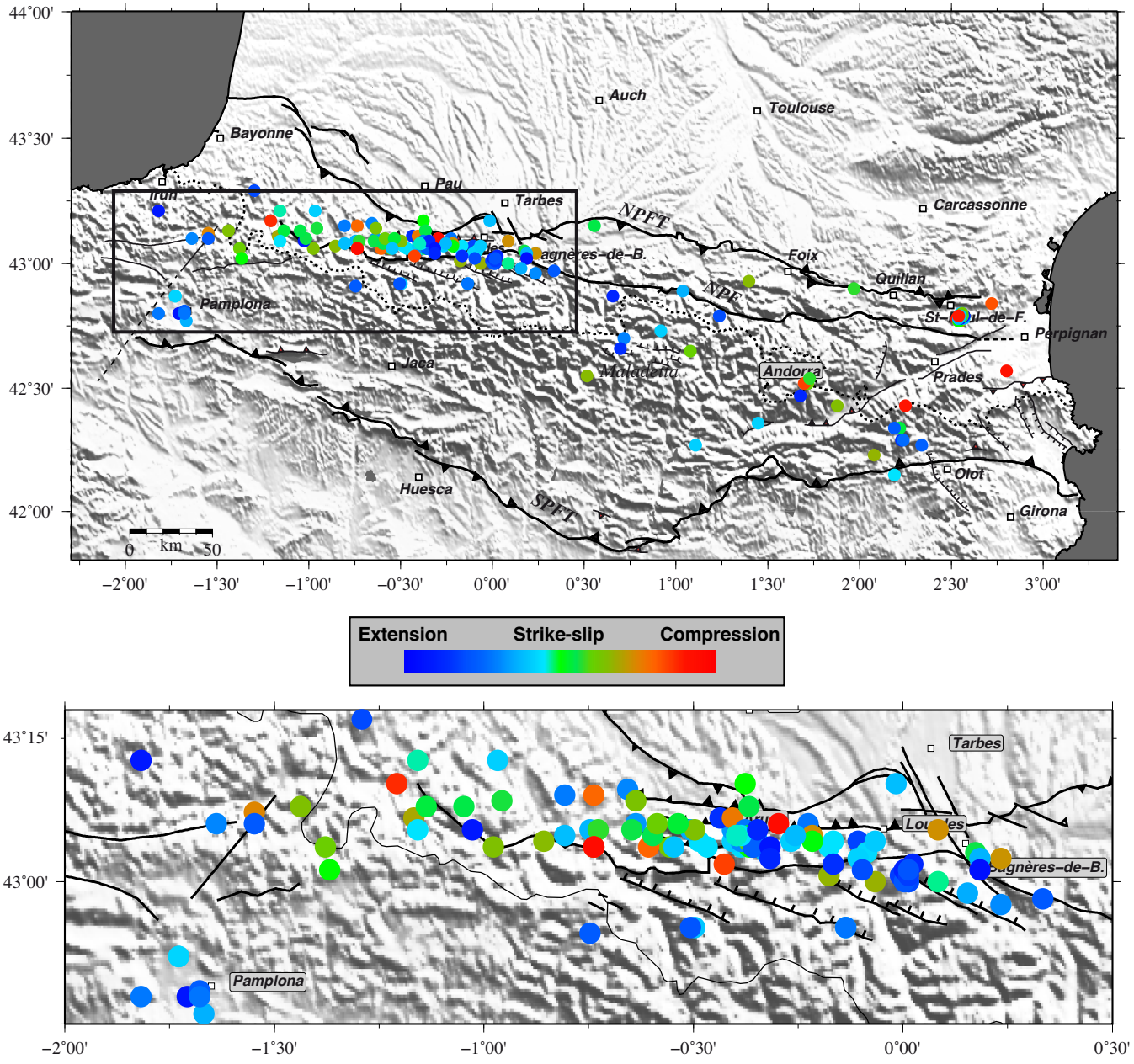

Figure 5. Map of 'r' factor on the shaded topographic map of Pyrenees (top), inset locates the close-up on the western part (bottom).

mainly striking E–W principally in the central part (south of the city of Tarbes). From this map, we infer that: (i) the deformation pattern is not uniform across the Pyrenees; (ii) extension is not the only mode of deformation; and (iii) there must be strong lateral variations in stress.

To characterize more precisely the Pyrenean deformation, we first analyse the focal mechanisms following the methodology proposed by Delacou *et al.* (2004), based on the plunge of the *P* and *T* axes. The *P* axes are vertical in an extensional domain whereas *T* axes are vertical in a compressional regime. If the plunges of the *P* and *T* axes are equal, then the stress field favours strike-slip faulting. Delacou *et al.* (2004) defined a factor *r* ranging from -90° for pure extension to 90° for pure compression, the null value corresponding to pure strike-slip. We mapped the *r* factor values, one per focal solution, in Fig. 5 (top) with an enlargement for the western part of the Pyrenees where the data are densest (Fig. 5, bottom).

Fig. 5 shows that the Pyrenean deformation field is more complex than uniform extension. Extension is apparent in the central part of the Pyrenees, in the area south of the city of Tarbes, including three of the four normal faults mapped by Lacan & Ortuño (2012). Two other areas of extension are identified: the area around the city of Pamplona in Spain, and an area to the east of the Pyrenees, near the city of Olot, consistent with the presence of NW–SE striking normal faults. A large E–W elongated area with a predominant strike-slip regime is identified in the western part of the range, southwest to the city of Pau. We also identify areas with compressional features in the eastern and western parts associated with strike-slip deformation patterns and probably indicating a transpressional deformation style. To the east, the compressional features correspond to the 1996 St-Paul-de-Fenouillet earthquake, where the main shock was a E–W left-lateral strike-slip mechanism and the aftershocks had mostly reverse-faulting mechanisms (Rigo *et al.* 1997; Pauchet *et al.* 1999).

6 STRESS AND STRAIN-RATE TENSORS

6.1 Stress tensors

To go further in the analysis of the focal mechanisms, we compute the stress tensors. We proceed by a fault-slip inversion using a Monte Carlo search method (Etchecopar *et al.* 1981) through the FSA software (Burg *et al.* 2005; Célérier 2011; Célérier *et al.* 2012). The inversion searches for the stress tensor that explains the majority of focal mechanisms. The magnitude of the events is not taken into account in the inversion. The focal mechanisms are given by one of the nodal planes. Then, we performed two inversions, the first one for the 'first' nodal plane chosen randomly, the second one with the other nodal plane. Next, we obtain the final stress tensor from a third inversion with the nodal planes, one per focal mechanism, having the smallest misfit in the previous two inversions. The uncertainty areas are defined from the five best solutions in each inversion. An inversion including all 194 focal mechanisms yields an extensional stress with the most compressive principal axis σ_1 oriented vertically and the least axis σ_3 oriented horizontally in the NE–SW direction (Table 3 and Fig. 6). This tensor is very similar to the one obtained by de Vicente *et al.* (2008), suggesting active N–S extension.

Because of the distribution of the seismicity and diversity of the focal mechanisms, we distinguish between the eastern and the western parts of the Pyrenees. In each part, we determine the stress tensor using the same method (Table 3 and Fig. 6). In the eastern part, the stress tensor shows a strike-slip regime where σ_1 and σ_3 are directed N–S and E–W, respectively, as also found by Goula *et al.* (1999). On the western side, extension dominates with σ_1 vertical and σ_3 horizontal but with a N–S direction instead. Fig. 5 demonstrates that the stress field varies across the Pyrenees, contradicting the uniformity assumed in previous studies (Nocquet & Calais 2004; de Vicente *et al.* 2008; Nocquet 2012). Consequently, we define eight zones where we estimate the stress tensors locally (Table 3, Fig. 6). This zoning is similar to the one proposed by Baize *et al.* (2013) based on the combination of geologic, seismologic and tectonic data to assess seismic hazard. The number of data in each zone varies. Zones 1, 5 and 6 include more than 30 focal mechanisms, whereas zones 2 and 7 include fewer than 10 data. Zone 4 is poorly constrained because it contains only 2 data. As shown in Fig. 6, three zones are in compression: zones 1 and 6 with N–S compression, zone 4 with E–W compression. Zone 6 includes E–W striking active reverse faults (Lacan & Ortuño 2012). Zones 3, 5 and 7 exhibit a predominance of strike-slip deformation style with extension and might be considered as transtensional areas. Zones 2 and 8 exhibit a pure extension regime with NE–SW and NNW–SSE direction, respectively. Zone 5 is of particular interest because the estimated σ_3 direction is compatible with the normal faults proposed by Lacan & Ortuño (2012).

Two other interesting points concern the σ_3 axis. First, σ_3 is the best-constrained component in each case studied. In other words, the uncertainty of σ_3 is less than those of either σ_1 or σ_2. Secondly, the σ_3 axis of least compressive stress is horizontal in all zones except zone 6. The σ_3 directions are consistent between zones 1, 2 and 3 in one group, zones 4 and 5 in another group, as well as zones 7 and 8 in a third group. This consistency and the stability of a horizontal σ_3 all over the range might explain why a purely extension stress tensor is obtained at the Pyrenean scale.

6.2 Seismic strain-rate tensors

In the following, we quantify the Pyrenean deformation by determining geodetic and seismic strain-rate tensors. We calculate the seismic strain-rate tensor according to the formulations of Kostrov (1974) and Jackson & McKenzie (1988), as used previously in different active regions (e.g. Masson *et al.* 2005). The average seismic strain rate $\dot{\varepsilon}_{ij}$ during a time interval Δt is:

$$\dot{\varepsilon}_{ij} = \frac{1}{2\mu \Delta t V} \sum_{n=1}^{N} M_{ij}^{n},$$

where μ is the modulus of rigidity, V is the crustal volume containing the seismic sources, and M_{ij}^{n} gives the components of the moment tensor M^n of earthquake n as calculated from the double-couple focal mechanism (Appendix Supplementary material). We assume the shear modulus $\mu = 3 \times 10^{10}$ Pa. We calculate the strain-rate tensors for the whole range, then for the eastern and western parts, and finally in each of the eight zones defined for the stress tensor determinations over a time span of 42.6 yr. To calculate the seismogenic volume V, we take its vertical dimension to be the maximum focal depth in each zone (Table 4). We also compute four different strain-rate tensors in each zone: one for the complete set of focal mechanisms for an elementary volume and without taking into account the magnitude (black strain-rate tensors in Fig. 7) to be directly compared in directions with the stress tensors shown in Fig. 6, one for the total set of focal mechanisms, one for the events with magnitude $M \geq 4.5$ (and $M < 5.7$) named high moment (HM) events, and finally one for the events with magnitude $M <$ 4.5 named low moment (LM) events. The focal mechanisms of the LM events are well constrained because they are determined from

Table 3. Principal stress axis S1 ($\sigma 1$, maximum), S2 ($\sigma 2$) and S3 ($\sigma 3$, minimum) resulting from FSA inversion. Nb f.m., number of focal mechanisms used in the inversion.

		S1		S2		S3	
Zone	Nb f.m.	Azimuth	Plunge	Azimuth	Plunge	Azimuth	Plunge
Total	195	86	82	314	5	223	45
East	71	351	17	128	67	256	14
West	124	217	60	110	10	15	28
1	47	15	27	125	33	255	44
2	7	306	37	166	45	53	21
3	15	307	66	178	15	83	17
4	2	267	21	113	65	1	10
5	69	294	16	119	73	24	1
6	35	213	8	122	8	346	78
7	13	229	34	110	35	349	36
8	7	225	63	77	23	342	12

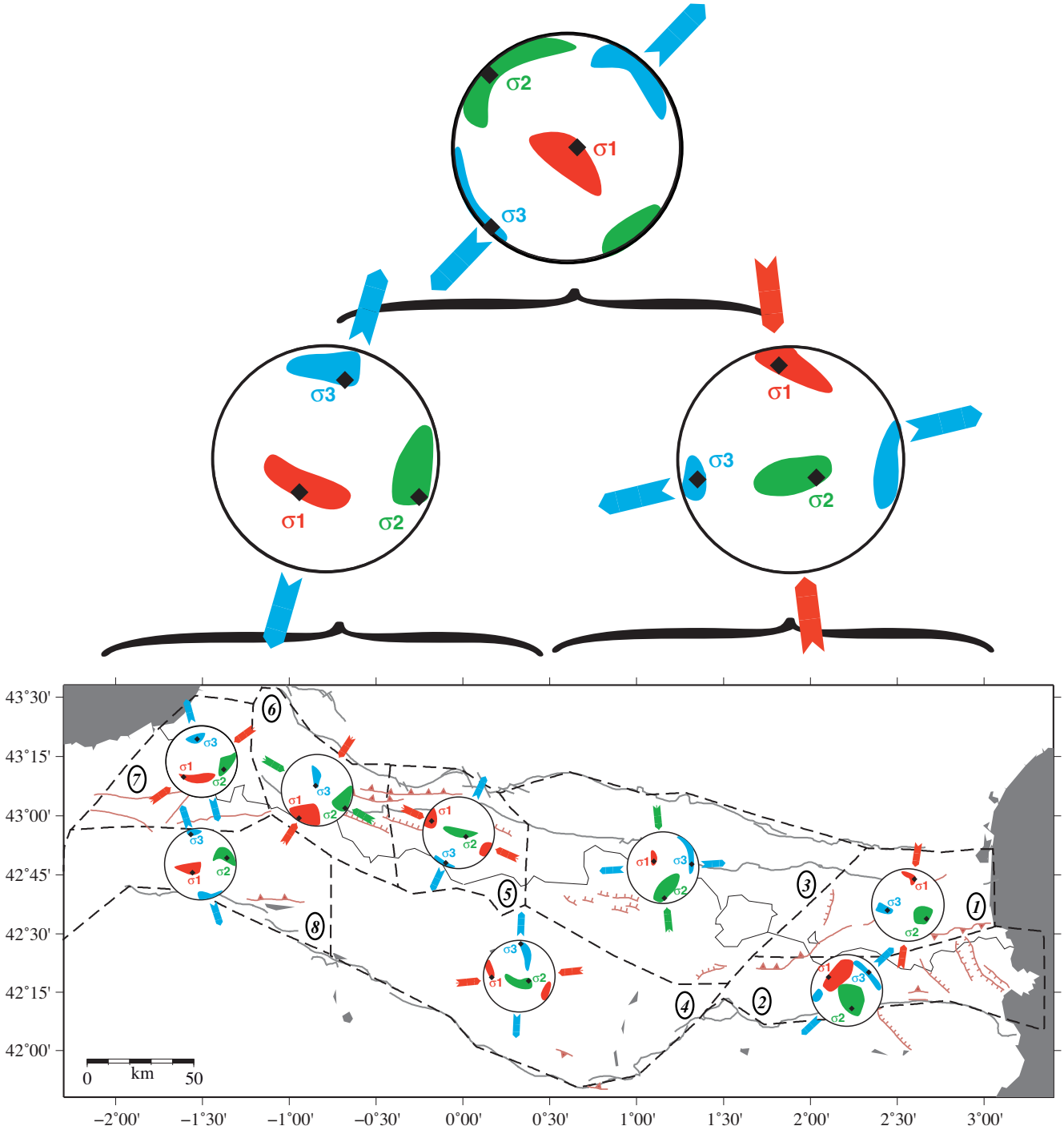

Figure 6. Stress tensors from FSA inversion. Colours correspond to the stress axis and their uncertainties: red $\sigma 1$; green $\sigma 2$ and blue $\sigma 3$. The active faults from Lacan & Ortuño (2012) are indicated in red.

local and/or temporary seismic networks. The HM events include 18 focal solutions, which is less than 10 per cent of our data set of focal mechanisms. Nevertheless, because of their HM, they will dominate the magnitudes and directions of the components of the strain-rate tensors. For this reason, we also determine the strain-rate tensors for the set of LM events to illustrate the deformation induced by this prevailing type of seismic event (90 per cent of the activity) in the Pyrenees.

The results for the horizontal components of the strain-rate tensors are shown in Table 4 and Fig. 7. As expected, the magnitudes of the strain rates for the complete data set (denoted (a) in Table 4 and Fig. 7) and for the HM events (denoted (b) in Table 4 and Fig. 7) are similar, ranging from 0.001 nstrain yr^{-1} to 9 nstrain yr^{-1}. The magnitudes of the strain rates for the LM events (denoted (c) in Table 4 and Fig. 7) are smaller by a factor of 10. Where the strain-rate tensors (a) and (b) are very similar, they are represented by a single tensor labelled (a and b) in Fig. 7. We note the consistency between the directions of horizontal components of the strain-rate tensor computed without the magnitude (black strain-rate tensors in Fig. 7) and the horizontal axis of the stress tensors shown in Fig. 6,

Table 4. Horizontal components of the strain-rate tensors. The vertical dimension of the seismogenic volume V is indicated between brackets and below at each zone. 1: amplitude of the first axis in nstrain/yr (negative is compression); 2: amplitude of the second axis in nstrain/yr (positive is extension); 3: azimuth of the second axis; Reduct. F.: reduction function value; a: all focal mechanisms; b: focal mechanisms with M $\geq$ 4.5 (HM events); c: focal mechanisms with M $<$ 4.5 (LM events); d: GPS with $\pm 2\sigma$, this study; e: GPS with $\pm 2\sigma$, Asensio et al. (2012). In brackets after a, b, c the number of focal mechanisms used.

Zone		1	2	3 (°)	Reduct. F.
	a (47)	−0.78	0.89	143	
1	b (1)	−0.74	0.91	144	
(11)	c (46)	−0.06	0.004	107	
	d	−17.59 ± 9.75	−2.13 ± 6.28	89 ± 29	0.75
	a (7)	0.01	0.28	49	
2	b (1)	−0.002	0.23	36	
(9)	c (6)	−0.024	0.09	80	
	d	−1.63 ± 6.50	25.25 ± 18.31	165 ± 23	0.85
	a (15)	0.02	0.04	73	
3	b (5)	0.02	0.04	87	
(17)	c (10)	−0.004	0.005	48	
	d	−3.90 ± 4.95	7.39 ± 5.93	136 ± 54	0.29
	a (2)	−0.01	0.005	177	
4	b (0)	–	–	–	
(5)	c (2)	−0.01	0.005	177	
	d	−23.28 ± 24.05	25.26 ± 25.28	73 ± 23	0.89
	a (69)	−1.88	2.31	127	
5	b (6)	−2.00	2.34	127	
(16)	c (63)	−0.04	0.14	21	
	d	−8.58± 9.83	29.43 ± 13.76	143 ± 13	1.06
	a (35)	−4.89	6.77	90	
6	b (4)	−6.50	9.01	90	
(20)	c (31)	−0.01	0.01	62	
	d	−9.22 ± 34.07	48. 40 ± 58.68	19 ± 47	0.81
	a (13)	−0.0002	0.0004	15.8	
7	b (0)	–	–	–	
(15)	c (13)	−0.0002	0.0004	15.8	
	d	–	–	–	
	a (7)	−0.12	0.61	7	
8	b (2)	−0.09	0.51	6	
(7)	c (5)	−0.03	0.10	8	
	d	−12.91 ± 15.91	21.27 ± 20.53	142 ± 58	1.18
all	a (195)	−0.22	0.36	109	
(20)	b (19)	−0.25	0.39	109	
	c (176)	−0.003	0.01	30	
	d	−0.86 ± 1.00	2.21 ± 1.69	169 ± 20	0.52
	e	0.77 ± 0.56	3.85 ± 1.79	21 ± 22	0.06
	a (71)	−0.02	0.07	142	
east	b (7)	−0.02	0.08	145	
(17)	c (64)	−0.006	0.006	78	
	d	−0.88 ± 1.38	0.62 ± 1.96	43 ± 72	0.39
	e	−0.06 ± 3.92	3.27 ± 2.84	164 ±76	0.42
	a (124)	−0.46	0.69	106	
west	b (12)	−0.55	0.79	106	
(20)	c (112)	−0.008	0.03	20	
	d	−1.37 ± 1.47	3.76 ± 1.94	155 ±14	0.54
	e	2.44 ± 1.61	4.46 ± 1.70	44 ± 81	0.25

except in zones 3 and 6. In zone 3, the directions of the horizontal components of the strain-rate tensor fall within the uncertainties of the stress tensor such that they can be considered consistent. For zone 6, the large discrepancy should be due to the large uncertainty in the estimate of the σ_1 axis of the stress tensor. The large discrepancies in direction between the strain-rate tensors without taking into account the magnitudes (black) and the strain-rate tensors labelled (a) are due to the predominance in the calculations of the mechanisms with the largest magnitudes.

For the whole Pyrenean chain, the strain-rate tensor for the LM events characterizes an extension regime with a NE–SW direction consistent with the corresponding stress tensor and with the results

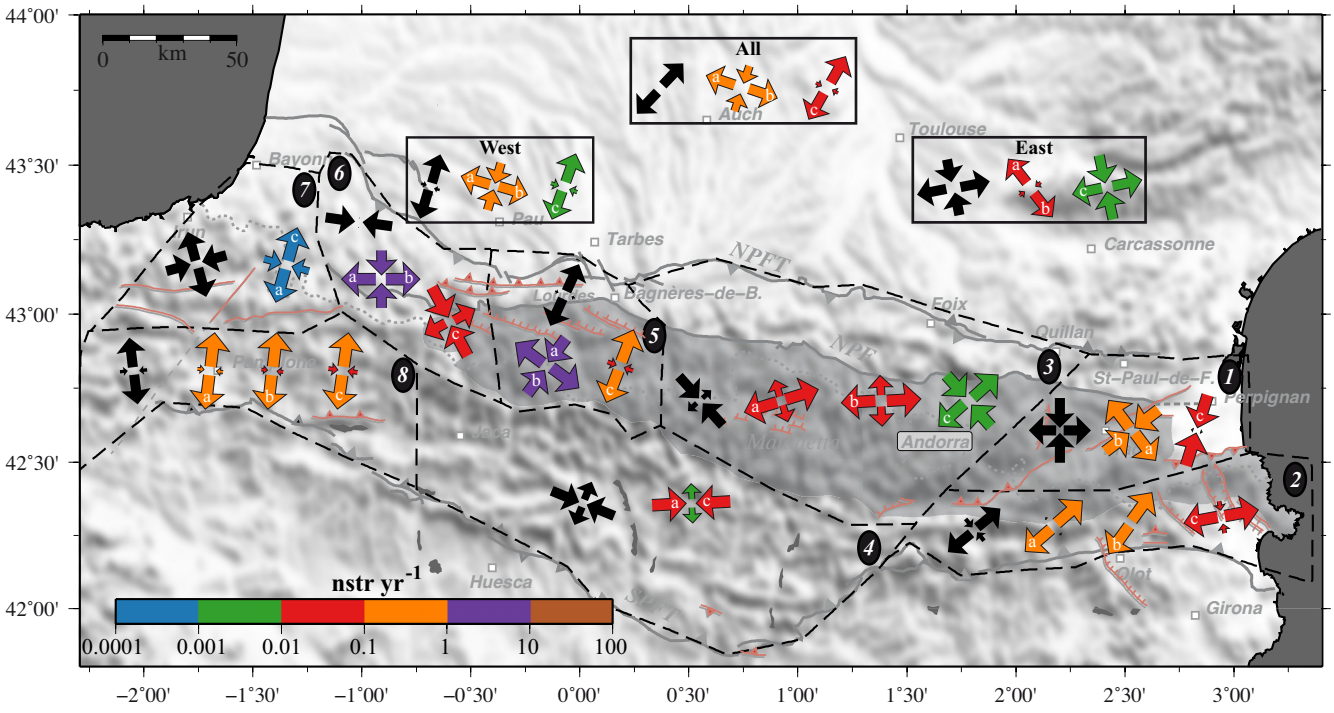

Figure 7. Seismic strain-rate tensors (Table 4). (a) All events; (b) HM events ($M \geq 4.5$); (c) LM events $M < 4.5$). In black, tensors are caluclated without magnitude in elementary volumes. Amplitudes of strain-rates are given by the coloured scale.

of de Vicente *et al.* (2008). In the cases (a) and (b) (all events and HM events, respectively), the strain-rate tensors are characteristic of a transtensional regime with a NW–SE extensional direction. The variability of the cases (a–b) and (c) is the expression of the geographical variability of the deformation style in the Pyrenees. This heterogeneity is noticeable when considering the eastern and western parts of the range. For the eastern region, the (a) and (b) cases have strain-rate tensors corresponding to NW–SE extension, whereas they correspond to strike-slip style in zone 1, to NE–SW extension style in zone 2, to E–W extension in zone 3 and to E–W compression in zone 4. Secondly, for case (c), the strain-rate tensors correspond to N–S compression in zone 1, E–W extension in zone 2, strike-slip in zone 3 and E–W compression in zone 4. For the western part of the Pyrenees, the strain-rate tensor for the (a) and (b) cases characterizes an E–W transtensional regime that combines the strike-slip styles in zones 5 and 6, and the extensional styles in zones 7 and 8. Case (c) shows strain-rate tensors with NE–SW extension for the western Pyrenean region and for zones 5, 7 and 8, but transpression in zone 6.

6.3 Geodetic strain-rate tensors

Even though the velocities estimated for individual GPS stations are negligible with 95 per cent confidence, we can group them together to determine the geodetic strain-rate tensors for a comparison with the seismic strain-rate tensors. The geodetic strain-rate tensor is the symmetric part of the 2-D tensor of the horizontal velocity gradient (Malvern 1969). These tensors are determined in each seismic zone according to the following method. To estimate a unique strain-rate tensor for each zone, we compute the linear trend of the velocity field, that minimizes the residual velocity on east and north components for all the GPS sites included in the zone. We then compute the spatial derivatives of this linear field which constitute the average velocity gradient over the zone. In order to verify if this tensor is significant, we compute up to 1000 strain-rate tensors by randomly perturbing the GPS velocities within their uncertainties. We then calculate the reduction function, which is the ratio of the mean wrms of the perturbed solutions to the wrms of the original GPS solution. A low value of the reduction function implies that even with small velocity perturbations, we find a velocity gradient similar to the original solution for the study area, hence the lower the value of the reduction function, the more significant the estimated strain-rate tensor. The results are given in Table 4, where they are denoted (d). Zone 7 has no strain-rate tensor determination because it includes only one GPS site. If the reduction function is greater than 0.7, then the corresponding strain-rate tensor is not well constrained because most of the 1000 perturbed solutions are statistically compatible with the originally velocity field. Table 4 shows that the reduction function values are less than 0.6 in only four areas: the western region, the eastern region, the whole Pyrenean range and zone 3. We plot only the first three strain-rate tensors with the corresponding velocity field in Fig. 8 (top). Zone 3 also has a small reduction function (0.29) indicating a NW–SE extension not consistent with the corresponding seismic strain-rate tensor obtained with diffuse and heterogeneous focal mechanisms.

Discrepancies exist between the velocity field estimated by Asensio *et al.* (2012) and our study. However this could be due to a misalignment of the reference frames. For an easier comparison, we compute the strain-rate tensors from the velocity field obtained by Asensio *et al.* (2012) and denoted (e) in Table 4. The strain-rate tensors are independent of the reference frame. In order to include their GPS stations, we extend the western region to the south. The velocity field from Asensio *et al.* (2012), modified to be in a reference frame similar to our study, and the strain-rate tensors are shown in Fig. 8 (bottom). The strain-rate tensors estimated from the two GPS data sets are similar and compatible within their respective uncertainties. From this comparison, we conclude that both velocity fields suggest a roughly NS extension.

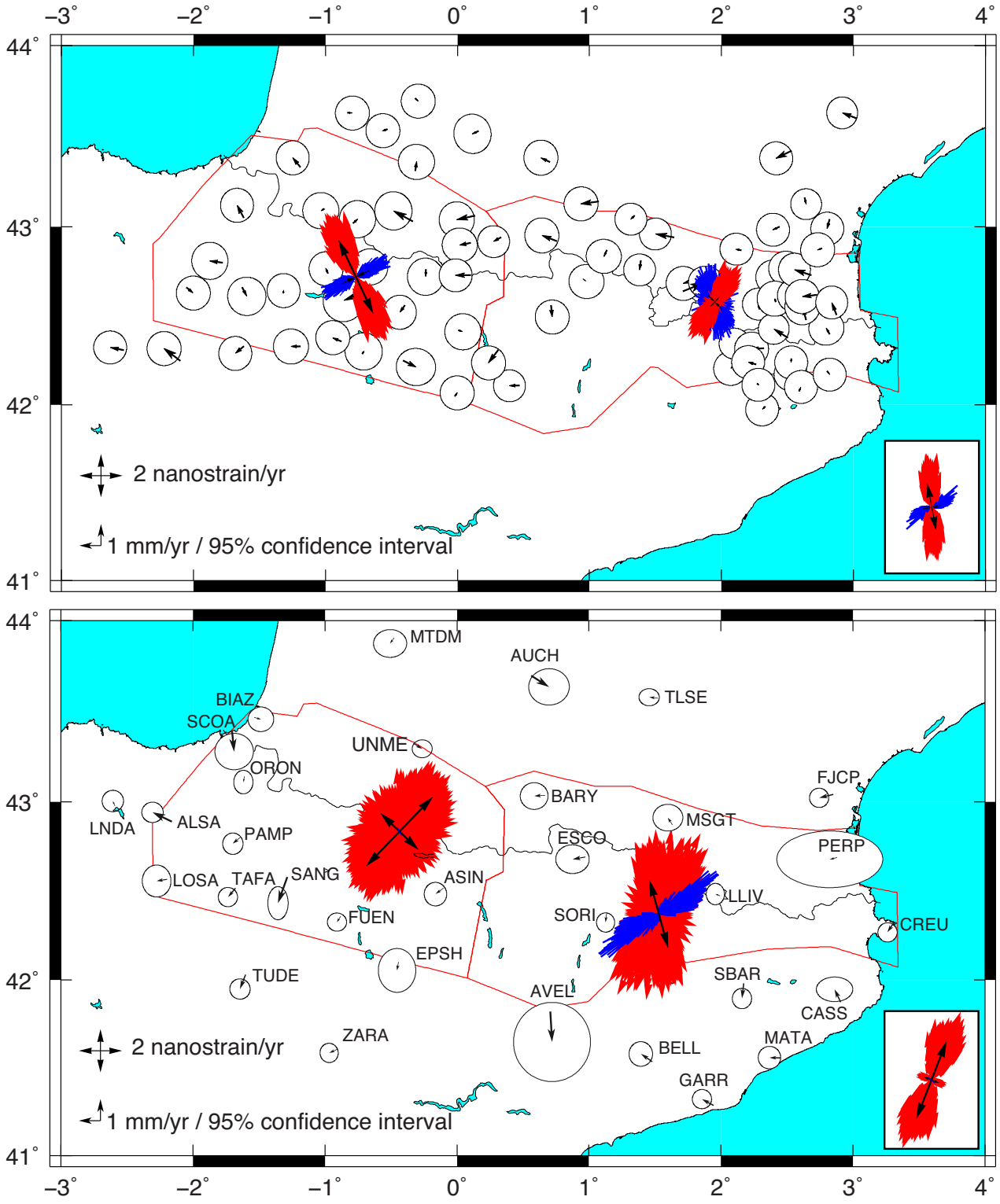

Figure 8. Geodetic strain-rate tensors (black, Table 4) for the eastern and western parts delimited by the red contour, and for the all Pyrenees in the inset. In red (extension axis) and blue (compression axis) are the 1000 tensors obtained by varying randomly the GPS velocities in their uncertainties (see text for details). Top: this study; bottom: from Asensio *et al.* (2012), the GPS velocities shown here being computed in the same European reference frame as our study.

The magnitudes of the geodetic estimates of strain rate, however, are slightly greater than the seismic estimates considering the HM events. On the other hand, they are consistent within the 2σ uncertainties, especially in zones 4, 5, 8 and for the whole Pyrenees range and for its western part (Table 4). Nevertheless, compared to the profiles (Fig. 3), the geodetic strain rates are consistent with the seismic ones for zones 1 and 2 with profiles AA′, and zones 5 and 6 with profile EE′. A deformation style of N–S extension seems to characterize the whole Pyrenees range in both cases. Transtension is apparent in the western region of the range with a NW–SE

extensional direction for our data and a NE–SW direction of greater extension for Asensio's observations, consistent with the overall seismic strain-rate tensor for all events and the HM subset within this zone. The eastern part of the range shows poorly constrained strain-rate tensors with a strike-slip deformation regime for our data and with NE–SW extension for Asensio's data.

The seismic catalogue we used spans only ∼40 yr, a small fraction (2 per cent) of the recurrence interval if of the order of ∼2500 yr for magnitude 6.5 earthquakes estimated from a previous study of geodetic strain rates spatially averaged over the entire Pyrenean range (Asensio *et al.* 2012). Since large earthquakes occur irregularly, any estimates of strain-rate and its attendant uncertainty that are based on seismicity are very likely to be biased by temporal aliasing. Furthermore, the assumption of a periodic or 'characteristic' earthquake is doubtful at best. In California, where the rate of deformation is arguably at least an order of magnitude faster than in the Pyrenees, large earthquakes occur on the San Andreas fault at irregular intervals with large variance in timing (Sieh *et al.* 1989). Similarly, extrapolating the deformation rate in time from the 1966 Parkfield earthquake failed to predict the next large earthquake there with 95 per cent confidence (Murray & Segall 2002).

Consequently, we compare the geodetic and seismic strain tensors in terms of spatial orientation rather than temporal rate. Such an approach has been used successfully in California, where the catalogue of earthquakes for which a centroid moment tensor can be calculated spans only a small fraction of the time since a large earthquake with magnitude greater than 7 on the San Andreas fault (e.g. Ekström & England 1989). Nonetheless, the 'orientations of relative velocity... determined from the seismicity between 1977 and 1987 agree within a few degrees with those determined from plate motions' (Ekström & England 1989). The approach is further justified mathematically by the fact that the orientation of the principal axis is the only directional quantity of the three required to define a horizontal strain rate tensor. Since this orientation does not involve time, it cannot be biased by temporal aliasing. Furthermore, a calculation including the focal mechanisms for small-magnitude earthquakes is likely to lead to an estimate of the orientation of the strain field that better represents the tectonic style than one neglecting them.

7 DISCUSSIONS AND CONCLUSION

We have analysed GPS surveys over the whole Pyrenean range at 74 sites spanning a time interval of 18 yr. The resulting velocity field (Fig. 2) shows that only a few of the velocities are significantly different from zero with 95 per cent confidence. Projected along profiles, only the westernmost N–S profile (profile EE′ in Fig. 3), with a deformation rate of 2.0 ± 1.8 nstrain yr^{-1}, approaches the value of 2.5 nstrain yr^{-1} given by Asensio *et al.* (2012). In the east, Asensio's study and ours show insignificant horizontal deformation rates. Moreover, since the measured networks include sites on both sides of the Pyrenees, we infer that the continental collision that generated this range appears now to have ceased to deform measurably. Thus, we conclude that the Iberian Plate is attached to the Eurasian one to within a few tenths of a millimetre per year.

Despite this very low deformation rate, we observe a diversity of deformational styles. Extension is principally present in the central part of the range, where most of the earthquakes analysed by de Vicente *et al.* (2008) and Chevrot *et al.* (2011) occur. The westernmost zone of the Pyrenees also exhibits extension, principally in the Spanish side around the city of Pamplona, with a predominant strike-slip regime. At the ends of the range, horizontal compression is apparent, especially in the eastern part, where the deformation is probably amplified by the 1996 seismic crisis of St-Paul-de-Fenouillet (Rigo *et al.* 1997; Pauchet *et al.* 1999; Rigo 2010). In the western part, an area of right-lateral strike-slip deformation regime (zone 6) connects two areas (zones 5 and 7–8) with perpendicular extension directions. This result suggests a rotation of the principal axis σ_2 from vertical to horizontal around a NE–SW horizontal σ_3 axis. This interpretation may explain why the fault-slip inversion of all focal mechanisms gives a stress tensor similar to the one obtained by de Vicente *et al.* (2008). We divide the Pyrenean range in eight zones in addition to the whole Pyrenees range and its western and eastern parts, for which we determined the seismic and geodetic stress and strain-rate tensors (Figs 6–8). Overall, the orientations of seismic stress and strain-rate tensors are consistent with the mapped active faults. Schematically, the Pyrenean deformation regime can be described as varying from transpression to the east to transtension to the west. Thus, deformation in the Pyrenees cannot be reduced to a single style but varies from east to west and from north to south over length scale of 20–40 km.

We conclude with three remarks. First, regarding the distribution of the seismicity, we note diffuse seismicity in the eastern part with a concentration at the Maladeta area, which is constituted by a granitic massif (Ortuño *et al.* 2008). In the central part of the range, the seismicity is principally located in the boundary zone between the North Pyrenean Zone and the Axial Zone. Since there is almost no seismic activity in the internal part of the range, this seismicity might be the expression of the deformation of the contact of two zones and not of the entire range. Because of the sparsity of seismicity, we cannot characterize or quantify the deformation at the northern and southern fronts of the Pyrenees. Measuring the rate of deformation there with geodetic techniques would require to resurvey the survey mode GPS networks and develop a denser network of continuously operating GNSS stations.

The second remark concerns the heterogeneity of the internal deformation of the Pyrenees, which is clear in Figs 5–7, where the style of deformation changes from one area to another. Since we divided the Pyrenees in zones according to seismicity and tectonics, the estimated strain-rate tensors capture the spatial complexity of the deformation field with a resolution of around 50 km. Camelbeeck *et al.* (2013) argued from the second derivative of the gravitational potential energy that the deformation styles in the Pyrenees may vary laterally over a few tens of kilometres. Although seismic and geodetic data cannot detect such details, but our and their observations are consistent, for example, in the central and eastern parts of the range with extension and strike-slip deformation styles, respectively.

Thirdly, we have analysed only the horizontal deformation. Further research is required to constrain the vertical motion in the Pyrenees. Although Giménez *et al.* (1996) analysed levelling data to find 1–4 mm yr^{-1} of uplift in the southeastern part of the range (Catalonia), Rigo & Cushing (1999) showed that there is no significant vertical movement along a short line in the central part of the range. However, with these fragmentary results, we cannot exclude the possibility of mostly vertical motion, as modelled by Vernant *et al.* (2013). To evaluate this possibility, it would be necessary to measure levelling lines across the Pyrenees to capture the differential vertical motion between the internal and higher part of the range and the forelands.

ACKNOWLEDGEMENTS

We are particularly grateful to the numerous participants to the GPS campaigns in the field, coming from ESGT, IRSN, IGN, ICGC and the universities of Toulouse, Montpellier and Barcelona. We thank Annie Souriau and Sébastien Chevrot for constructive discussions. We thank R.W. King and an anonymous reviewer for their pertinent and very helpful comments on the manuscript. This work benefited from the instruments of Parc GPS INSU and from the financial support of the Tectoscope Positionnement, PNRN, 3F and CT3 programs from INSU/CNRS and of the Regional Council of Midi-Pyrénées and of Cataluña Province. The figures were prepared using the Generic Mapping Tool GMT (Wessel & Smith 1991).

REFERENCES

Alasset, P.J. & Meghraoui, M., 2005. Active faulting in the Western Pyrenees (France): paleoseismic evidence for late Holocene ruptures, *Tectonophysics,* **409,** 39–54.

Asensio, E., Khazaraddze, G., Echeverria, A., King, R.W. & Vilajosana, I., 2012. GPS studies of active deformation in the Pyrenees, *Geophys. J. Int.,* **190,** 913–921.

Baize, S., Cushing, E., Lemeille, F. & Jomard, H., 2013. Updated seismotectonic zoning scheme of Metropolitan France, with reference to geologic and seismotectonic data, *Bull. Soc. géol. Fr.,* **184,** 225–259.

Bardainne, T., Dubos-Sallée, N., Sénéchal, G., Gaillot, P. & Perroud, H., 2008. Analysis of the induced seismicity of the Lacq gas field (Southwestern France) and model of deformation, *Geophys. J. Int.,* **172,** 1151–1162.

Briais, A., Armijo, R., Winter, T., Tapponnier, P. & Herbecq, A., 1990. Morphological evidence for Quaternary normal faulting and seismic hazard in the eastern Pyrenees, *Annales Tectonicae,* **IV,** 19–42.

Burg, J.-P., Célérier, B., Chaudhry, N.M., Ghazanfar, M., Gnehm, F. & Schnellmann, M., 2005. Fault analysis and paleostress evolution in large strain regions: methodological and geological discussion of the southeastern Himalayan fold-and-thrust belt in Pakistan, *J. Asian Earth Sci.,* **24,** 445–467.

Calvet, M., 1999. Régime des contraintes et volumes de relief dans l'est des Pyrénées, *Géomorphologie: relief, processus, environnement,* **3,** 253–278.

Camelbeeck, T., de Viron, O., Van Camp, M. & Kusters, D., 2013. Local stress sources in Western Europe lithosphere from geoid anomalies, *Lithosphere,* **5,** 235–246.

Campanyà, J., Ledo, J., Queralt, P., Marcuello, A., Liesa, M. & Munoz, J.A., 2011. Lithospheric characterization of the Central Pyrenees based on new magnetotelluric data, *Terra Nova,* **23,** 213–219.

Campanyà, J., Ledo, J., Queralt, P., Marcuello, A., Liesa, M. & Munoz, J.A., 2012. New geoelectrical characterisation of a continental collision zone in the West-Central Pyrenees: constraints from long periiod and broadband magnetotellurics, *Earth planet. Sci. Lett.,* **333–334,** 112–121.

Cansi, Y., Ménéchal, Y. & Santoire, J.P., 1988. *Sismicité des Pyrénées 1962–1985 – Doc. LDG/TD-G/390/88, Laboratoire de Détection Géophysique,* Commissariat à l'Énergie Atomique, Bruyères-le-Châtel, France, p. 43.

Carozza, J.M. & Delcaillau, B., 2000. Réponse des bassins versants à l'activité tectonique: l'exemple de la terminaison orientale de la chaîne pyrénéenne. Approche morphotectonique, *Géomorphologie,* **1,** 45–60.

Célérier, B., 2011. *FSA: Fault and Stress Analysis Software, version 33.8,* Univ. Montpellier 2, Montpellier, France. Available at: http://www.pages-perso-bernard-celerier.univmontp2.fr/software/dcmt/fsa/fsa.html.

Célérier, B., Etchecopar, A., Bergerat, F., Vergely, P., Arthaud, F. & Laurent, P., 2012. Inferring stress from faulting: from early concepts to inverse methods, *Tectonophysics,* **581,** 206–219.

Chevrot, S., Sylvander, M. & Delouis, B., 2011. A preliminary catalog of moment tensors for the Pyrenees, *Tectonophysics,* **510,** 239–251.

Chevrot, S. *et al.*, 2014. High-resolution imaging of the Pyrenees and Massif Central from the data of the PYROPE and IBERARRAY portable array deployments, *J. geophys. Res.: Solid Earth,* **119,** 6399–6420.

Choukroune, P., 1992. Tectonic evolution of the Pyrenees, *Annu. Rev. Earth planet. Sci.,* **20,** 143–158.

Daignières, M., Seguret, M., Specht, M. & ECORS team, 1994. The Arzacq-Western Pyrenees ECORS deep seismic profile, *Publ. Eur. Assoc. Pet. Geol.,* **4,** 199–208.

Delacou, B., Sue, C., Champagnac, J.-D. & Burkhard, M., 2004. Present-day geodynamics in the bend of the western and central Alps as constrained by earthquake analysis, *Geophys. J. Int.,* **158,** 753–774.

Delouis, B., Haessler, H., Cisternas, A. & Rivera, L., 1993. Stress tensor determination in France and neighbouring regions, *Tectonophysics,* **221,** 413–437.

de Vicente, G., Cloetingh, S., Munoz-Martin, A., Olaiz, A., Stich, D., Vegas, R., Galindo-Zaldivar, J. & Fernandez-Lozano, J., 2008. Inversion of moment tensor focal mechanisms for active stresses around the microcontinent Iberia: tectonic implications, *Tectonics,* **27,** TC1009, doi: 10.1029/2006TC002093.

Dong, D., Herring, T.A. & King, R.W., 1998. Estimating regional deformation from a combination of space and terrestrial geodetic data, *J. Geodesy,* **72,** 200–214.

Dubos, N., Sylvander, M., Souriau, A., Ponsolles, C., Chevrot, S., Fels, J.-F. & Benahmed, S., 2004. Analysis of the May 2002 earthquake sequence in Central Pyrenees, consequences for the evaluation of the seismic risk at Lourdes, France, *Geophys. J. Int.,* **156,** 527–540.

Dubos-Sallée, N., Nivière, B., Lacan, P. & Hervouët, Y., 2007. A structural model for the seismicity of the Arudy (1980) epicentral area (Western Pyrenees, France), *Geophys. J. Int.,* **171,** 259–270.

Durá-Gómez, I. & Talwani, P., 2010. Reservoir-induced seismicity associated with the Itoiz Reservoir, Spain: a case study, *Geophys. J. Int.,* **181,** 343–356.

Ekström, G. & England, P., 1989. Seismic strain rates in regions of distributed continental deformation, *J. geophys. Res.,* **94,** 10 231–10 257.

Etchecopar, A., Vasseur, G. & Daignières, M., 1981. An inverse problem in microtectonics for the determination of stress tensors from fault striation analysis, *J. Struct. Geol.,* **3,** 51–65.

Feigl, K.L. *et al.*, 1993. Space geodetic measurement of crustal deformation in central and southern California, 1984–1992. *J. geophys. Res.,* **98,** 21677–21712.

Fleta, J., Soro, M., Gimenez, J. & Suriñach, E., 1996. Red GPS para medidas geodinámicas en el Pirineo (ResPyr), *Geogaceta,* **20,** 992–995.

Gagnepain-Beyneix, J., 1987. *Étude expérimentale des tremblements de terre. Exemple de la region d'Arette (France),* PhD Thesis, Univ. Paris VII, p. 220.

Gagnepain-Beyneix, J., Haessler, H. & Modiano, T., 1982. The pyrenean earthquake of February 29, 1980: an example of complex faulting, *Tectonophysics,* **85,** 273–290.

Gagnepain, J., Modiano, T., Cisternas, A., Ruegg, J. C., Vadell, M., Hatzfeld, D. & Mezcua, J., 1980. Sismicité de la région d'Arette (Pyrénées-Atlantiques) et mécanismes au foyer, *Ann. Géophys.,* **36,** 499–508.

Gallart, J., Banda, E. & Daignères, M., 1981. Crustal structure of the Paleozoic Axial Zone of the Pyrenees and transition to the North Pyrenean Zone, *Ann. Geophys.,* **37,** 457–480.

Gallart, J., Olivera, C., Daignières, M. & Hirn, A., 1982. Quelques données récentes sur la relation entre fractures crustales et séismes dans les Pyrénées Orientales, *Bull. Soc. Géol. Fr.,* **XXIV,** 293–298.

Gallart, J., Daignères, M., Gagnepain-Beyneix, J., Hirn, A. & Olivera, C., 1984. Seismostructural studies in the Pyrenees: evolution and recent results, *Pageoph.,* **122,** 713–724.

Gallart, J., Daignières, M., Gagnepain-Beyneix, J. & Hirn, A., 1985. Relationship between deep structure and seismicity in the western Pyrenees, *Ann. Geophys.,* **3,** 239–248.

Giménez, J., Surinach, E., Fleta, J. & Goula, X., 1996. Recent vertical movements from high-precision leveling data in northeast Spain, *Tectonophysics,* **263,** 149–161.

Goula, X., Talaya, J., Termens, A., Colomina, I., Fleta, J., Grellet, B. & Granier, T., 1996. Avaluació de la potencialitat sísmica del Pirineu Oriental: primers resultats de les campanyes GPS PotSis'92 i PotSis'94, *Revista Catalana de Geografia,* **11,** 41–48.

Goula, X., Olivera, C., Fleta, J., Grellet, B., Lindo, R., Rivera, L.A., Cisternas, A. & Carbon, D., 1999. Present and recent stress regime in the eastern part of the Pyrenees, *Tectonophysics,* **308,** 487–502.

Grandjean, G., 1992. Mise en évidence des structures crustales dans une portion de chaine et de leur relation avec les bassins sédimentaires. *Application aux Pyrénées occidentales au travers du projet ECORS Arzacq-Pyrénées,* PhD Thesis, Univ. Montpellier II.

Grandjean, G., Daignières, M., Gallart, J. & Hirn, A., 1994. Répartition de la sismicité dans la partie occidentale des Pyrénées, *C. R. Acad. Sci.,* **319,** 527–533.

Guilbert, J., 1992. Localisation et étude de la sismicité sous la Maladeta, Rapp. *Stage Magistère ENS Lyon, Observatoire Midi-Pyrénées,* p. 56.

Herring, T., 2003. MATLAB tools for viewing GPS velocities and time series, *GPS Solutions,* **7,** 194–199.

Hirn, A., Daignères, M., Gallart, J. & Vadell, M., 1980. Explosion seismic sounding of throws and dips in the continental Moho, *Geophys. Res. Lett.,* **7,** 263–266.

Hoang Trong, P. & Rouland, D., 1971. Mécanisme au foyer du séisme d'Arette, Pyrénées Atlantique, *C. R. Acad. Sci.,* **272,** 3249–3251.

Jackson, J.A. & McKenzie, D.P., 1988. The relationship between plate motions and seismic tensors, and the rates of active deformation in the Mediterranean and Middle East, *Geophys. J. R. astr. Soc.,* **93,** 45–73.

Jammes, S., Lavier, L.L. & Manatschal, G., 2010. Extreme crustal thinning in the Bay of Biscay and the Western Pyrenees: from observations to modeling, *Geochem. Geophys. Geosyst.,* **11,** Q10016, doi: 10.1029/2010GC003218.

Kostrov, B., 1974. Seismic moment and energy of earthquakes and seismic flow of rocks, *Izv. Acad. Sci. USSR, Phys. Solid Earth,* **1,** 23–40.

Lacan, P. & Ortuño, M., 2012. Active tectonics of Pyrenees: a review, *J. Iberian Geol.,* **38,** 9–30.

Lacan, P., Nivière, B., Rousset, D. & Sénéchal, P., 2012. Late Pleistocene folding above the Mail Arrouy Thrust, North-Western Pyrenees (France), *Tectonophysics,* **541,** 57–68.

Lambert, J. & Levret-Albaret, A., 1996. *Mille ans de séismes en France,* Ouest Éditions, Nantes, p. 75.

Ledo, J., Ayala, C., Pous, J., Queralt, P., Marcuello, A. & Munoz, J.A., 2000. New geophysiscal constraints on the deep structure of the Pyrenees, *Geophys. Res. Lett.,* **27,** 1037–1040.

Malvern, L.E., 1969. *Introduction to the Mechanics of a Continuum Medium,* Prentice-Hall.

Masson, F., Chéry, J., Hatzfeld, D., Martinod, J., Vernant, P., Tavakoli, F. & Ghafory-Ashtiani, M., 2005. Seismic versus aseismic deformation in Iran inferred from earthquakes and geodetic data, *Geophys. J. Int.,* **160,** 217–226.

Murray, J. & Segall, P., 2002. Testing time-predictable earthquake recurrence by direct measurement of strain accumulation and release, *Nature,* **419,** 287–291.

Nicolas, M., Santoire, J.P. & Delpech, P.Y., 1990. Intraplate seismicity: new seismotectonic data in western Europe, *Tectonophysics,* **179,** 27–53.

Nocquet, J.-M., 2012. Present-day kinematics of the Mediterranean: a comprehensive overview of GPS results, *Tectonophysics,* **579,** 220–242.

Nocquet, J.-M. & Calais, E., 2004. Geodetic measurements of crustal deformation in the western Mediterranean and Europe, *Pure appl. Geophys.,* **161,** 661–681.

Olivera, C. & Gallart, J., 1987. Sismicidad de la region de Navarra (Pireneos occidentales), *Rev. de Geofisica,* **43,** 221–234.

Olivera, C., Susagna, T., Fleta, J., Roca, A. & Goula, X., 1992. Seismicity of the Valencia trough and surrounding areas, *Tectonophysics,* **203,** 99–109.

Olivera, C., Redondo, E., Lambert, J., Riera, A. & Roca, A., 2006. The earthquakes of the XIV and XV centuries in Catalonia (NE Spain), *in First European Conference on Earthquake Engeneering and Seismology,* Geneva, Switzerland.

Ortuño, M., Queralt, P., Marti, A., Ledo, J., Masana, E., Perea, H. & Santanach, P., 2008. The North Maladeta Fault (Spanish Central Pyrenees) as the Vielha 1923 earthquake seismic source: recent activity revealed by geomorpholoqical and geophysical research, *Tectonophysics,* **453,** 246–262.

Pauchet, H., Rigo, A., Rivera, L. & Souriau, A., 1999. A detailed analysis of the February 1996 aftershock sequence in the eastern Pyrenees, France, *Geophys. J. Int.,* **137,** 107–127.

Perea, H., 2009. The Catalan seismic crisis (1427 and 1428; NE Iberian Peninsula): Geological sources and earthquake triggering, *J. Geodyn.,* **47,** 259–270.

Philip, H., Bousquet, J.C., Escuer, J., Fleta, J., Goula, X. & Grellet, B., 1992. Présence de failles inverses d'âge quaternaire dans l'Est des Pyrénées: implications sismotectoniques, *C. R. Acad. Sci. Paris,* **314,** 1239–1245.

Pous, J., Ledo, J., Marcuello, A. & Daignères, M., 1995. Electrical resistivity model of the crust and upper mantle from a magnetotelluric survey through the central Pyrenees, *Geophys. J. Int.,* **121,** 750–762.

Reilinger, R. *et al.*, 2006. GPS constraints on continental deformation in the Africa Arabia Eurasia continental collision zone and implications for the dynamics of plate interactions, *J. geophys. Res.,* **111,** 2156–2202.

Rigo, A., 2010. Precursors and fluid flows in the case of the 1996, ML = 5.2 Saint-Paul-de-Fenouillet earthquake (Pyrenees, France): a complete pre-, co- and post-seismic scenario, *Tectonophysics,* **480,** 109–118.

Rigo, A. & Cushing, M., 1999. Effets topographiques sur les comparaisons de profils de nivellement: cas français de Saint-Paul-de-Fenouillet (Pyrénées-Orientales) et d'Arudy (Pyrénées-Atlantiques), *C.R. Acad. Sci. Paris,* **329,** 697–704.

Rigo, A. & Massonnet, D., 1999. Investigating the 1996 Pyrenean earthquake (France) with SAR interferograms heavily distorted by atmosphere, *Geophys. Res. Lett.,* **26,** 3217–3220.

Rigo, A., Pauchet, H., Souriau, A., Grésillaud, A., Nicolas, M., Olivera, C. & Figueras, S., 1997. The February 1996 earthquake sequence in the eastern Pyrenees: first results, *J. Seismol.,* **1,** 3–14.

Rigo, A., Souriau, A., Dubos, N., Sylvander, M. & Ponsolles, C., 2005. Analysis of the seismicity in the central part of the Pyrenees (France), and tectonic implications, *J. Seismol.,* **9,** 211–222.

Ruiz, M., Gaspà, O., Gallart, J., Diaz, J., Pulgar, J.A., Garcia-Sansegundo, J., Lopez-Fernandez, C. & Gonzalez-Cortina, J.M., 2006a. Aftershocks series monitoring of the September 18, 2004 M = 4.6 earthquake at the western Pyrenees: a case of reservoir-triggered seismicity?, *Tectonophysics,* **424,** 223–243.

Ruiz, M., Gallart, J., Diaz, J., Olivera, C., Pedreira, D., Lopez, C., Gonzalaz-Cortina, J.M. & Pulgar, J.A., 2006b. Seismic activity at the western Pyrenean edge, *Tectonophysics,* **412,** 217–235.

Sieh, K., Stuiver, M. & Brillinger, D., 1989. A more precise chronology of earthquakes produced by the San Andreas fault in southern California, *J. geophys. Res.,* **94,** 603–623.

Smith, W.H.F. & Wessel, P., 1990. Gridding with continuous curvature splines in tension, *Geophysics,* **55,** 293–305.

Souriau, A. & Granet, M., 1995. A tomographic study of the lithosphere beneath the Pyrenees from local and teleseismic data, *J. geophys. Res.,* **100,** 18 117–18 134.

Souriau, A. & Pauchet, H., 1998 A new synthesis of Pyrenean seismicity and its tectonic implications, *Tectonophysics,* **290,** 221–244.

Souriau, A., Chevrot, S. & Olivera, C., 2008. A new tomographic image of the Pyrenean lithosphere from teleseismic data, *Tectonophysics,* **460,** 206–214.

Souriau, A., Sylvander, M., Rigo, A., Fels, J.-F., Douchain, J.-M. & Ponsolles, C., 2001. Sismotectonique des Pyrénées: principales contraintes sismologiques, *Bull. Soc. géol. Fr.,* **172,** 25–39.

Stich, D., Serpelloni, E., Mancilla, F.L. & Morales, J., 2006. Kinematics of the Iberia-Maghreb plate contact from seismic moment tensors and GPS observations, *Tectonophysics,* **426,** 295–317.

Stich, D., Martin, R. & Morales, J., 2010. Moment tensor inversion for Iberia-Maghreb earthquakes 2005–2008, *Tectonophysics,* **483,** 390–398.

Sylvander, M., Souriau, A., Rigo, A., Tocheport, A., Toutain, J. P., Ponsolles, C. & Benahmed, S., 2008. The November 2006, $M_L = 5.0$ earthquake near Lourdes (French Pyrenees): normal faulting in an active mountain belt, *Geophys. J. Int.,* **175,** 649–664.

Talaya, J., Feigl, K., Térmens, A. & Colomina, I., 1999. Practical lessons from analysis of a GPS network designed to detect movements of = 1 mm/year in the eastern Pyrenees, *Phys. Chem. Earth,* **24,** 355–359.

Torné, M., Cabissole, B.D., Bayer, R., Casas, A., Daignières, M. & Rivero, A., 1989. Gravity constraints on the deep structure of the Pyrenean belt along the ECORS profile, *Tectonophysics,* **165,** 105–116.

Vacher, P. & Souriau, A., 2001. A three-dimensional model of the Pyrenean deep structure based on gravity modelling, seismic images and petrological constraints, *Geophys. J. Int.,* **145,** 460–470.

Vernant, P., Hivert, F., Chéry, J., Steer, P., Cattin, R. & Rigo, A., 2013. Erosion-induced isostatic rebound triggers extension in low convergent mountain ranges, *Geology,* **41,** 467–470.

Vissers, R.L.M. & Meijer, P.T., 2012. Iberian plate kinematics and Alpine collision in the Pyrenees, *Earth-Sci. Rev.,* **114,** 61–83.

Wessel, P. & Smith, W.H.F., 1991. Free software helps map and display data, *EOS, Trans. Am. geophys. Un.,* **72**(41), 441–446.

SUPPORTING INFORMATION

Additional Supporting Information may be found in the online version of this paper:

Appendix
(http://gji.oxfordjournals.org/lookup/suppl/doi:10.1093/gji/ggv052/-/DC1).

Please note: Oxford University Press is not responsible for the content or functionality of any supporting materials supplied by the authors. Any queries (other than missing material) should be directed to the corresponding author for the paper.